ELSEVIER

Contents lists available at ScienceDirect

Computer Physics Communications

journal homepage: www.elsevier.com/locate/cpc



On a novel fully-decoupled, linear and second-order accurate numerical scheme for the Cahn-Hilliard-Darcy system of two-phase Hele-Shaw flow^{*}



Xiaofeng Yang

Department of Mathematics, University of South Carolina, Columbia, SC 29208, USA

ARTICLE INFO

Article history:
Received 6 June 2020
Received in revised form 2 December 2020
Accepted 29 January 2021
Available online 27 February 2021

Keywords:
Second-order
Phase-field
Cahn-Hilliard
Darcy
Unconditional energy stability
Fully-decoupled

ABSTRACT

We construct a novel fully-decoupled and second-order accurate time marching numerical scheme with unconditional energy stability for the Cahn-Hilliard-Darcy phase-field model of the two-phase Hele-Shaw flow, in which, the key idea to realize the full decoupling structure is to use the so-called "zero-energy-contribution" function and design a special ordinary differential equation to deal with the nonlinear coupling terms between the flow field and the phase-field variable. Compared with the existing decoupling type schemes, the scheme developed here is more effective, efficient and easy to implement. At each time step, one only needs to solve a few fully-decoupled linear equations only with constant coefficients. We also strictly prove the solvability and unconditional energy stability of the scheme, and implement various numerical simulations in 2D and 3D to show the efficiency and stability of the proposed scheme numerically.

© 2021 Elsevier B.V. All rights reserved.

1. Introduction

In this paper, we consider the numerical approximations of the Cahn-Hilliard-Darcy phase-field model of the two-phase Hele-Shaw flow system (CHD, for short). The term Hele-Shaw (or Hele-Shaw cells) is commonly used to describe the motions of viscous fluids which is limited by two parallel plates with a very small gap. For this type of flow, the fluid motion conforms to the mechanical principles in porous media, and the boundary conditions are defined by the pressure. Starting with the pioneering work in [1], the Cahn-Hilliard equation describing the two-phase flows is coupled with the Darcy equations to simulate the motion of the two-phase fluid flow confined in two flat plates, in which both fluids are assumed to be inertialess. Similar models had also been used to describe tumor growth, see [2,3]. Although the CHD model has received extensive attention, as a complex nonlinear system, to develop easy-to-implement, accurate, and unconditional energy stable schemes for solving it is still very challenging. The main difficulty lies on how to discretize the following three terms, (i) the coupling of the velocity and phase-field function through the nonlinear advection and surface tension; (ii) the stiffness term related to the interfacial width due to the nonlinear double-well potential; and (iii) the coupling between the velocity and pressure through the divergence-free condition in the Darcy equation.

The difficulty referred in (ii) means that for a nonlinear term that causes stiffness, simple implicit or explicit type discretization may lead to strict stability constraints on the time step (cf. [4,5]), resulting in practical inefficiency. We recall that many successful efforts have been made in the direction of designing appropriate discretization for nonlinear terms to obtain unconditionally energy stable schemes. Some well-known methods include, but are not limited to: the convex splitting [6-11], the linear stabilization [5,12,13], the Invariant Energy Quadratization (IEQ) [14–17] and its various version of the Scalar Auxiliary Variable (SAV) [18–20], nonlinear implicit derivative [21], nonlinear quadrature [22-24] methods, etc. Therefore, it can be considered that the difficulty (ii) has been solved well. The difficulty mentioned in (iii) can also be easily solved by the direct method [25,26], or the projection-type method [27-34]. Therefore, we can also consider that it has been solved well.

Regarding the difficulty referred to in (i), we recall that there is also a successful scheme developed in [11,28] that can achieve the full decoupling structure, second-order time accuracy, and unconditional energy stability. Its key idea is to use the convex-splitting method to deal with the double-well potential and the way of implicit-explicit combination to deal with the advection and surface tension. For this scheme, we temporarily ignore its relatively expensive computational cost due to the nonlinearity and only discuss the decoupling method developed therein. It is worth noting that the implicit-explicit combination used in [11,28] to deal with advection and surface tension is a very common method that has been widely adopted to deal with

The review of this paper was arranged by Prof. Hazel Andrew. E-mail address: xfyang@math.sc.edu.

the same terms that appear in the Cahn-Hilliard-Navier-Stokes system (referred to as CH-NS) for two-phase flow, cf. [10,11,13, 14,34-37]. However, for the CH-NS system, this method can only generate a fully-coupled scheme. Hence, a natural question arises: when dealing with the same terms in the same way, what causes the completely different result, that is, the fully-decoupled scheme for the CHD model and the fully-coupled scheme for the CH-NS model? The answer is contained in the special format of the Darcy equation, where the pressure gradient and velocity satisfy an explicit linear relationship. Therefore, the fluid velocity can be given explicitly by the pressure, so as to achieve a fully-decoupled scheme. However, in the Navier-Stokes equation, there is no similar explicit relationship between the velocity and pressure gradient at all. Therefore the way of the implicit and explicit combination of advection and surface tension will inevitably lead to a fully-coupled scheme.

Therefore, in this paper, we aim to construct a novel full decoupling scheme for the CHD model. This scheme does not require an explicit relationship between the velocity and pressure, and can also achieve the fully-decoupling and second-order accuracy. We expect the scheme to be linear and unconditionally energy stable as well. To achieve the full decoupling structure, we take advantage of a well-known but often overlooked special property, the so-called "zero-energy-contribution" feature [38-42] satisfied by the two coupling terms advection and surface tension. When deducing the energy law, if a proper test function is selected to perform the inner product, these two coupling terms will cancel each other out. In other words, the contribution of these two terms to the energy is zero. We apply this property and develop a novel way to deal with these terms, by adding a specially designed ordinary differential equation (ODE) to the system that contains the inner product of these nonlinear terms. This ODE is trivial at the continuous level because all the terms in it are zero. But after discretization, it can help eliminate all the troublesome nonlinear terms to obtain unconditional energy stability. Besides, the nonlocal variable can be used to decompose all equations into two sub-equations which can be solved independently. As a result, the fully-decoupled feature is achieved.

After combining this novel decoupling method with the projection type method for the Darcy fluid equation, and the SAV method that is used to linearize the nonlinear double-well potential, we arrive at an effective numerical scheme with all the desired properties (linear, fully-decoupling, second-order accurate in time, and unconditionally energy stable). Although the developed scheme is not the first and unique fully-decoupled scheme for solving the CHD model, compared with the scheme in [11,28], it has two advantages. First, the scheme in [28] uses the convex-splitting method, and its nonlinear nature requires more time expense (cf. Fig. 4.7 (b)), while the scheme developed here is linear and very effective in practice because we only need to solve a few fully-decoupled elliptic equations with constant coefficients at each time step. Second, the scheme developed in [28] utilizes the special property of the Darcy equation, so it is difficult to generalize to other type of fluid coupling system, while the new decoupling method can be used to construct efficient numerical schemes for many coupled nonlinear models, not only the Darcy equation considered in this paper but also the Navier-Stokes equations [14,43], magnetic field [44], electric field [45,46], heat equations [17,47], etc.

The rest of the article is organized as follows. We briefly describe the CHD model and derive its energy structure in Section 2. In Section 3, a fully decoupled numerical scheme is constructed, and then its implementation is described in detail. The solvability and unconditional energy stability are proved rigorously as well. In Section 4, we implement the developed scheme and test its accuracy/stability by simulating plenty of 2D and 3D examples. Some concluding remarks are given in Section 5.

2. Cahn-Hilliard-Darcy system

Now, we briefly introduce the Cahn–Hilliard–Darcy phase-field model for the two-phase Hele–Shaw flow system. Suppose that Ω is a smooth, open bounded, connected domain in \mathbb{R}^d , d=2,3. Let $\phi(\mathbf{x},t)$ be a phase-field variable (or called labeling function) to represent the volume fraction of the two distinct fluid components in the fluid mixture, i.e.,

$$\phi(x,t) = \begin{cases} 1 & \text{fluid } 1, \\ -1 & \text{fluid } 2, \end{cases}$$
 (2.1)

with a thin, smooth transition region with a width $O(\epsilon)$. The total free energy is postulated as a combination of the gradient potential and Ginzburg–Landau type double-well functional:

$$E(\phi) = \int_{\Omega} \lambda (\frac{1}{2} |\nabla \phi|^2 + F(\phi)) d\mathbf{x}, \tag{2.2}$$

where $F(\phi) = \frac{1}{4\epsilon^2}(\phi^2 - 1)^2$, λ accounts for the surface tension parameter. The gradient entropy acts as the hydrophilic type of interaction (the tendency to mix), and the double-well potential represents the hydrophobic type of interaction (the tendency to separate).

Assuming that the fluid motion conforms to the mechanical principles in porous media and follows the generalized Fick's law of mass flux proportional to the chemical potential gradient, the Cahn-Hilliard-Darcy model reads as:

$$\phi_t + \nabla \cdot (\mathbf{u}\phi) = M\Delta\mu, \tag{2.3}$$

$$\mu = \lambda(-\Delta\phi + f(\phi)),\tag{2.4}$$

$$\tau \mathbf{u}_t + \alpha \mathbf{u} + \nabla p + \phi \nabla \mu = 0, \tag{2.5}$$

$$\nabla \cdot \mathbf{u} = 0, \tag{2.6}$$

where **u** is the nondimensionalized seepage velocity, $f(\phi) = F'(\phi) = \frac{1}{\epsilon^2}(\phi^3 - \phi)$, τ is a positive parameter, M is the mobility parameter, p is the pressure, α is the dimensionless hydraulic conductivity. Note the time derivative of the seepage velocity **u** is retained for flows in porous medium, cf. [11,28,48,49].

We consider one of the following two types of boundary conditions or their combination:

(ii)
$$\mathbf{u} \cdot \mathbf{n}|_{\partial\Omega} = \partial_{\mathbf{n}} \phi|_{\partial\Omega} = \partial_{\mathbf{n}} \mu|_{\partial\Omega} = 0,$$
 (2.7)

where ${\bf n}$ is the unit outward normal on the boundary $\partial \Omega$. Remarkably, if the boundary conditions are (ii), then it is easy to derive that

$$\partial_{\mathbf{n}} p|_{\partial \Omega} = 0. \tag{2.8}$$

The initial conditions read as

$$\mathbf{u}|_{(t=0)} = \mathbf{u}^{0}, \ p|_{(t=0)} = p^{0}, \ \phi|_{(t=0)} = \phi^{0}. \tag{2.9}$$

The system (2.3)–(2.6) admits the law of energy dissipation which can be derived by the following process. By multiplying the inner product of (2.3) with $-\mu$ in L^2 , we derive

$$-(\phi_t, \mu) = M \|\nabla \mu\|^2 + \int_{\Omega} \nabla \cdot (\mathbf{u}\phi) \mu d\mathbf{x}. \tag{2.10}$$

By taking the L^2 inner product of (2.4) with ϕ_t , we obtain

$$(\mu, \phi_t) = \frac{d}{dt} \int_{\Omega} (\frac{\lambda}{2} |\nabla \phi|^2 + \lambda F(\phi)) d\mathbf{x}. \tag{2.11}$$

By taking the L^2 inner product of (2.5) with **u** and using integration by parts and (2.6), we obtain

$$\frac{d}{dt} \int_{\Omega} \frac{\tau}{2} |\mathbf{u}|^2 d\mathbf{x} + \alpha ||\mathbf{u}||^2 + \int_{\Omega} \phi \nabla \mu \cdot \mathbf{u} d\mathbf{x} = 0.$$
 (2.12)

By combining the above three equalities, we obtain the energy law as follows,

$$\frac{d}{dt}E(\mathbf{u},\phi) = -M\|\nabla\mu\|^2 - \alpha\|\mathbf{u}\|^2,$$
(2.13)

where the two negative terms on the right end prescribe the energy diffusive rate and

$$E(\mathbf{u},\phi) = \int_{\Omega} \left(\frac{\tau}{2}|\mathbf{u}|\right)^2 + \lambda \left(\frac{1}{2}|\nabla\phi|^2 + F(\phi)\right) d\mathbf{x}.$$
 (2.14)

Remark 2.1. When deriving the PDE energy law (2.13), the two nonlinear terms are canceled by using integration by parts, namely,

$$\int_{\mathcal{Q}} (\phi \nabla \mu \cdot \mathbf{u} + \nabla \cdot (\mathbf{u}\phi)\mu) d\mathbf{x} = 0.$$
 (2.15)

This shows that the advection and surface tension terms have no contribution to the total free energy or energy diffusivity. Therefore, the "zero-energy-contribution" feature behind these two terms inspires us to design a fully decoupled scheme, which will be given in the next section.

We fix some notations here. For each $k \geq 0$, let $(\cdot, \cdot)_k$ and $\|\cdot\|_k$ be the $H^k(\Omega)$ inner product and norm, respectively $(H^0(\Omega) = L^2(\Omega))$. We use (\cdot, \cdot) and $\|\cdot\|$ to denote the L^2 inner product and its norm, respectively. For any given integer N>0, we set $\delta t=T/N$ as the time step, and set ψ^n as the numerical approximation of the value of solution $\psi(\cdot, t)$ at $t=t^n=n\delta t$, $0\leq n\leq N$.

3. Numerical scheme

This section aims to construct a time marching scheme to solve the CHD system (2.3)-(2.6) and it is expected to be fullydecoupled, linear, second-order accurate, and unconditionally energy stable. To this end, we introduce a new method in this paper, the main idea of which is to combine several approaches that have been proved to be effective. First, the projection-type method is used to discretize the Darcy equations. Second, for the nonlinear term $f(\phi)$, we use the recently developed SAV approach in which an auxiliary variable is used to convert the nonlinear part of the energy to a quadratic form. This approach helps us to obtain a linear scheme. Third, for advection and surface tension terms with the "zero-energy-contribution" property, we introduce a second auxiliary variable and a trivial ODE associated with it. This method brings three benefits. First, the modified system is equivalent to the original system. Second, the coupled nonlinear terms can be dealt with explicitly when discretizing the system. Third, this variable decomposes all equations into multiple independent sub-equations that can be solved independently, thereby achieving the full-decoupling. The detailed process is shown as follows.

First, we introduce a nonlocal auxiliary variable Q(t) and design a special ODE that reads as

$$\begin{cases}
Q_t = \int_{\Omega} (\nabla \cdot (\mathbf{u}\phi)\mu + (\phi\nabla\mu) \cdot \mathbf{u}) d\mathbf{x}, \\
Q|_{(t=0)} = 1,
\end{cases}$$
(3.1)

 $\mathbf{u} \cdot \mathbf{n}|_{\partial \Omega} = \mathbf{0}$, or all variables are periodic.

It is easy to derive that the ODE (3.1) is equivalent to a trivial ODE $(Q_t = 0, Q|_{(t=0)} = 1)$ which has the solution of Q(t) = 1.

Second, we define the first nonlocal auxiliary variable U(t) as a square root of the integral of the double-well potential, that read as

$$U = \sqrt{\int_{\Omega} F(\phi) d\mathbf{x} + B},\tag{3.2}$$

where *B* is a constant ensuring a positive radian. This is the so-called SAV method that is very efficient to linearize the nonlinear terms induced by the free energy potential.

Then, by using the two nonlocal variables Q, U, and combining the ODE system (3.1) with the CHD system (2.3)–(2.6), we obtain the following equivalent form:

$$\phi_t + Q\nabla \cdot (\mathbf{u}\phi) = M\Delta\mu,\tag{3.3}$$

$$\mu = \lambda(-\Delta\phi + HU),\tag{3.4}$$

$$U_t = \frac{1}{2} \int_{\Omega} H \phi_t d\mathbf{x},\tag{3.5}$$

$$\tau \mathbf{u}_t + \alpha \mathbf{u} + \nabla p + Q \phi \nabla \mu = 0, \tag{3.6}$$

$$\nabla \cdot \mathbf{u} = 0, \tag{3.7}$$

$$Q_t = \int_{\Omega} (\nabla \cdot (\mathbf{u}\phi)\mu + (\phi\nabla\mu) \cdot \mathbf{u}) \, d\mathbf{x}, \tag{3.8}$$

where

$$H(\phi) = \frac{f(\phi)}{\sqrt{\int_{\Omega} F(\phi) d\mathbf{x} + B}}.$$
(3.9)

The transformed system (3.3)–(3.8) in the new variables $(\mathbf{u}, p, \phi, \mu, Q, U)$ forms a closed PDE system with the following initial conditions,

$$\mathbf{u}|_{(t=0)} = \mathbf{u}^{0}, \ p|_{(t=0)} = p^{0}, \ \phi|_{(t=0)} = \phi^{0},$$

$$Q|_{(t=0)} = 1, \ U|_{(t=0)} = \sqrt{\int_{\Omega} F(\phi^{0}) d\mathbf{x} + B}.$$
(3.10)

Note the two Eqs. (3.5) and (3.8) for the new variables U, Q are only differential equations in time, hence the boundary conditions of the new system (3.3)–(3.8) are still (2.7).

Remark 3.1. The new system (3.3)–(3.8) is exactly equivalent to the original PDE system (2.3)–(2.6) since the summation of two nonlinear integral terms in (3.8) is equal to zero by using integration by parts, which means Q(t) = 1. Therefore, we multiply Q to the advection term $\nabla \cdot (\mathbf{u}\phi)$ and the surface tension $\phi \nabla \mathbf{u}$ will not change anything of the system. Meanwhile, after integrating (3.5) with time t and using the initial condition (3.10), we directly get (2.4).

The transformed system (3.3)–(3.8) also follows an energy dissipative law which can be derived by a similar process to obtain (2.13). We present the details here since the discrete energy stability proof follows the same approach. We multiply the L^2 inner product of (3.3) with μ to get

$$(\phi_t, \mu) + M \|\nabla \mu\|^2 + \underbrace{Q \int_{\Omega} \nabla \cdot (\mathbf{u}\phi) \mu d\mathbf{x}}_{l_1} = 0.$$
(3.11)

By taking the L^2 inner product of (3.4) with ϕ_t , we obtain

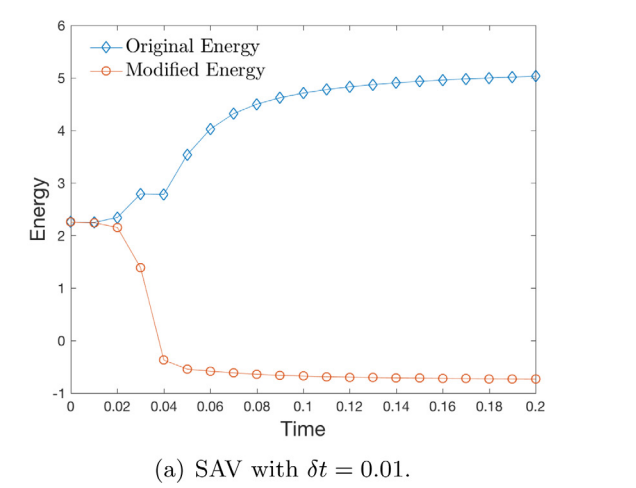
$$-(\mu,\phi_t) + \frac{d}{dt} \int_{\Omega} \frac{\lambda}{2} |\nabla \phi|^2 d\mathbf{x} + \lambda U \int_{\Omega} H \phi_t d\mathbf{x} = 0.$$
 (3.12)

By taking the L^2 inner product of (3.5) with $2\lambda U$, we obtain

$$\frac{d}{dt}(\lambda U^2) - \lambda U \int_{\Omega} H\phi_t d\mathbf{x} = 0.$$
 (3.13)

By taking the L^2 inner product of (3.6) with **u** and using (3.7), we obtain

$$\frac{d}{dt} \int_{\Omega} \frac{\tau}{2} |\mathbf{u}|^2 d\mathbf{x} + \alpha \|\mathbf{u}\|^2 + \underbrace{Q \int_{\Omega} (\phi \nabla \mu) \cdot \mathbf{u} d\mathbf{x}}_{\text{U}} = 0.$$
 (3.14)



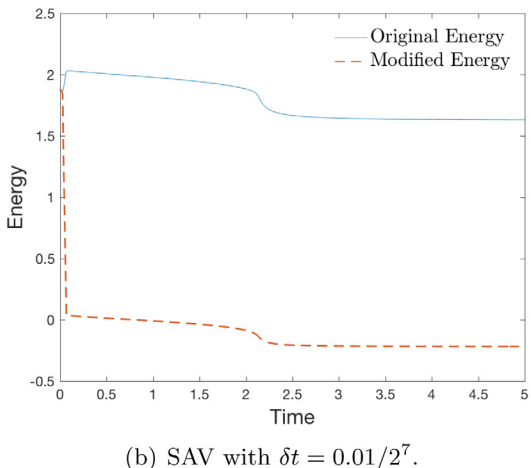


Fig. 4.1. Stability tests computed by the scheme SAV ((3.17)–(3.23) with S=0) with two different time steps (a) $\delta t=0.01$ and (b) $\delta t=0.01/2^7$, where the original energy (2.14) and modified energy (3.57) are plotted in each subfigure.

By taking the L^2 inner product of (3.8) with Q, we obtain

$$\frac{d}{dt}(\frac{Q^2}{2}) = \underbrace{Q\int_{\Omega}\nabla\cdot(\mathbf{u}\phi)\mu d\mathbf{x}}_{l_2} + \underbrace{Q\int_{\Omega}(\phi\nabla\mu)\cdot\mathbf{u}d\mathbf{x}}_{l_2}.$$
(3.15)

By combining the above five equalities and noting that the terms I_1 and I_2 , II_1 and II_2 are canceled respectively, we obtain the energy law as follows,

$$\frac{d}{dt} \left(\int_{\Omega} \left(\frac{\tau}{2} |\mathbf{u}|^2 + \frac{\lambda}{2} |\nabla \phi|^2 \right) d\mathbf{x} + \lambda U^2 + \frac{Q^2}{2} \right)$$

$$= -M \|\nabla \mu\|^2 - \alpha \|\mathbf{u}\|^2 \le 0.$$
(3.16)

Remark 3.2. The advantages of adding a simple ordinary differential equation for Q can be seen from the above energy law derivation process. Note that the term I_1 is offset by term I_2 , and term II_1 is offset by term II_2 . In this way, we can use different methods to discretize I_1 and II_1 because they no longer need to cancel each other out, making it possible to design a fully-decoupled scheme.

Now, we are ready to develop a numerical scheme to solve (3.3)–(3.8). Based on the second-order backward differentiation formula (BDF2), a time marching scheme is constructed as follows.

We compute $\tilde{\mathbf{u}}^{n+1}$, \mathbf{u}^{n+1} , ϕ^{n+1} , μ^{n+1} , U^{n+1} , Q^{n+1} by

$$\frac{a\phi^{n+1} - b\phi^n + c\phi^{n-1}}{2\delta t} + Q^{n+1}\nabla \cdot (\mathbf{u}^*\phi^*) = M\Delta\mu^{n+1}, \tag{3.17}$$

$$\mu^{n+1} = \lambda(-\Delta\phi^{n+1} + H^*U^{n+1} + \frac{S}{\epsilon^2}(\phi^{n+1} - \phi^*)), \tag{3.18}$$

$$aU^{n+1} - bU^{n} + cU^{n-1}$$

$$= \frac{1}{2} \int_{\Omega} H^{*}(a\phi^{n+1} - b\phi^{n} + c\phi^{n-1}) d\mathbf{x},$$
(3.19)

$$\tau \frac{a\tilde{\mathbf{u}}^{n+1} - b\mathbf{u}^n + c\mathbf{u}^{n-1}}{2\delta t} + \alpha \tilde{\mathbf{u}}^{n+1}$$

$$+\nabla p^{n} + Q^{n+1}\phi^{*}\nabla\mu^{*} = 0,$$

$$Q^{n+1} - bQ^{n} + cQ^{n-1}$$
(3.20)

$$= \int_{\Omega} \left(\nabla \cdot (\mathbf{u}^* \phi^*) \mu^{n+1} + (\phi^* \nabla \mu^*) \cdot \tilde{\mathbf{u}}^{n+1} \right) d\mathbf{x}, \tag{3.21}$$

and

$$\tau \frac{a}{2\delta t} (\mathbf{u}^{n+1} - \tilde{\mathbf{u}}^{n+1}) + \nabla (p^{n+1} - p^n) = 0, \tag{3.22}$$

$$\nabla \cdot \mathbf{u}^{n+1} = 0, \tag{3.23}$$

where

$$a = 3, b = 4, c = 1,$$

 $\mathbf{u}^* = 2\mathbf{u}^n - \mathbf{u}^{n-1}, \phi^* = 2\phi^n - \phi^{n-1},$
 $\mu^* = 2\mu^n - \mu^{n-1}, H^* = H(\phi^*),$ (3.24)

S > 0 is a pre-assigned stabilization parameter. We set the boundary conditions to be periodic or

$$\partial_{\mathbf{n}} p^{n+1}|_{\partial \Omega} = \partial_{\mathbf{n}} \phi^{n+1}|_{\partial \Omega} = \partial_{\mathbf{n}} \mu^{n+1}|_{\partial \Omega} = \mathbf{u}^{n+1} \cdot \mathbf{n}|_{\partial \Omega} = 0.$$
 (3.25)

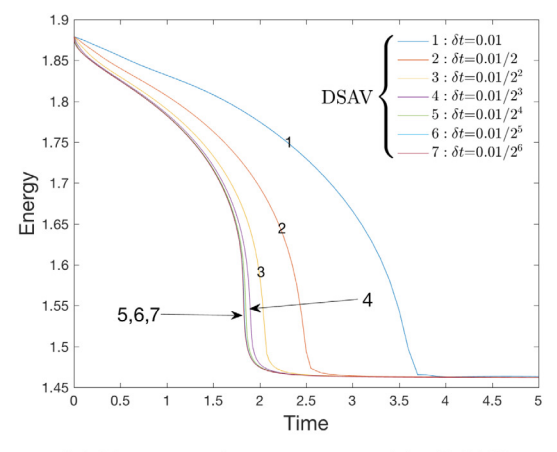
Remark 3.3. A second-order pressure-correction scheme is used to decouple the computation of the pressure from that of the velocity, see [11,27,28,28–34,50]. The initialization of the second-order scheme requires the values of all variables at $t=t^1$, which can be obtained by constructing a first-order scheme using the backward Euler method. In the above second-order scheme (3.17)–(3.23), by setting a=2, b=2, c=0, and $\psi^*=\psi^0$ for any variable ψ , the first-order scheme can be easily obtained.

Remark 3.4. We add an extra second-order linear stabilization term related to *S* in (3.18). Although this term introduces extra error of $\frac{s}{\epsilon^2}\delta t^2 \partial_{tt}\phi(\cdot)$, its magnitude is comparable with the error caused by the second-order extrapolated nonlinear term $f(\phi)$. In Section 4, we present sufficient numerical evidence that the stabilizer is essential for maintaining accuracy and improving the energy stability while using large time steps, see the accuracy/stability tests shown in Fig. 4.1, 4.2, and 4.6 (cf. [20]).

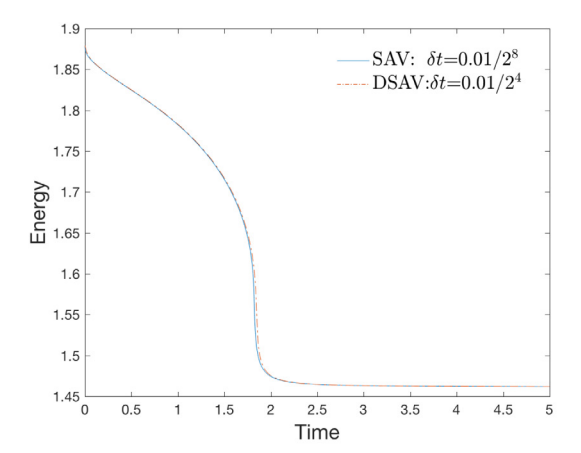
However, it seems that the scheme (3.17)–(3.23) is not a fully-decoupled scheme we expect. It looks more like a fully-coupled scheme, instead. Since all variables are related tightly, it may require expensive iterative solvers in practical computations. To achieve the fully-decoupled implementation, we need take advantage of the nonlocal properties of U and Q. We do not need to explicitly solve them, but use them to divide all variables into several equations that can be solved independently. In this way, as long as by solving several linear equations with constant coefficients, the final solution can be obtained, which can greatly reduce the actual computational cost. The specific implementation process is as follows.

First, we use the nonlocal scalar variable Q^{n+1} to split $(\phi, \mu, U)^{n+1}$ into a linear combination that reads as

$$\begin{cases} \phi^{n+1} = \phi_1^{n+1} + Q^{n+1}\phi_2^{n+1}, \\ \mu^{n+1} = \mu_1^{n+1} + Q^{n+1}\mu_2^{n+1}, \\ U^{n+1} = U_1^{n+1} + Q^{n+1}U_2^{n+1}. \end{cases}$$
(3.26)



(a) Energy evolution computed by DSAV.



(b) Energy evolution computed by SAV and DSAV.

Fig. 4.2. (a) Stability tests computed by DSAV with seven different time steps, where the original energy (2.14) is plotted. (b) The evolutions over time of the total free energy (2.14) computed by SAV with $\delta t = 0.01/2^8$ and DSAV with $\delta t = 0.01/2^4$.

Then the scheme (3.17)–(3.18) can be rewritten as

$$\begin{cases} \frac{a}{2M\delta t}(\phi_{1}^{n+1} + Q^{n+1}\phi_{2}^{n+1}) + \frac{1}{M}Q^{n+1}\nabla \cdot (\mathbf{u}^{*}\phi^{*}) \\ = \Delta(\mu_{1}^{n+1} + Q^{n+1}\mu_{2}^{n+1}) \\ + \frac{1}{2M\delta t}(b\phi^{n} - c\phi^{n-1}), \\ \mu_{1}^{n+1} + Q^{n+1}\mu_{2}^{n+1} = \left(-\lambda\Delta + \frac{S}{\epsilon^{2}}\right)(\phi_{1}^{n+1} + Q^{n+1}\phi_{2}^{n+1}) \\ + H^{*}(U_{1}^{n+1} + Q^{n+1}U_{2}^{n+1}) - \frac{S}{\epsilon^{2}}\phi^{*}, \end{cases}$$
(3.27)

According to Q^{n+1} , the linear system (3.27) can be decomposed into two sub-systems as follows:

$$\begin{cases} \frac{a}{2M\delta t}\phi_1^{n+1} = \Delta\mu_1^{n+1} + A_1, \\ \mu_1^{n+1} = \left(-\lambda\Delta + \frac{S}{\epsilon^2}\right)\phi_1^{n+1} + H^*U_1^{n+1} + B_1, \end{cases}$$
(3.28)

$$\begin{cases} \frac{a}{2M\delta t}\phi_2^{n+1} = \Delta\mu_2^{n+1} + A_2, \\ \mu_2^{n+1} = \left(-\lambda\Delta + \frac{S}{\epsilon^2}\right)\phi_2^{n+1} + H^*U_2^{n+1}, \end{cases}$$
(3.29)

where A_1, A_2, B_1 are explicit, that read as

$$A_1 = \frac{1}{2M\delta t}(b\phi^n - c\phi^{n-1}), B_1 = -\frac{S}{\epsilon^2}\phi^*, A_2 = -\frac{1}{M}\nabla \cdot (\mathbf{u}^*\phi^*).$$

Note that the two subsystems (3.28) and (3.29) have the same form, so we only need to introduce a method to solve any one of them, and the other follows the same rule. We take the first subsystem (3.28) as an example. To solve (3.28), we continue to use the split technique, that is, the variables $(\phi_1, \mu_1)^{n+1}$ are split into a linear combination form by the variable U_1^{n+1} which read as

$$\phi_1^{n+1} = \phi_{11}^{n+1} + U_1^{n+1}\phi_{12}^{n+1}, \mu_1^{n+1} = \mu_{11}^{n+1} + U_1^{n+1}\mu_{12}^{n+1}. \tag{3.30}$$

By substituting the split form of all variables in (3.30) into (3.28) and decomposing the results according to U_1^{n+1} , we obtain two independent subsystems that read as

$$\begin{cases} \frac{a}{2M\delta t}\phi_{11}^{n+1} = \Delta\mu_{11}^{n+1} + A_1, \\ \mu_{11}^{n+1} = \left(-\lambda\Delta + \frac{S}{\epsilon^2}\right)\phi_{11}^{n+1} + B_1, \end{cases}$$
(3.31)

$$\begin{cases} \frac{a}{2M\delta t}\phi_{12}^{n+1} = \Delta\mu_{12}^{n+1}, \\ \mu_{12}^{n+1} = \left(-\lambda\Delta + \frac{S}{\epsilon^2}\right)\phi_{12}^{n+1} + H^*, \end{cases}$$
(3.32)

The boundary conditions for (3.31)–(3.32) are either periodic or

$$\partial_{\mathbf{n}}\phi_{11}^{n+1}|_{\partial\Omega} = \partial_{\mathbf{n}}\phi_{12}^{n+1}|_{\partial\Omega} = \partial_{\mathbf{n}}\mu_{11}^{n+1}|_{\partial\Omega} = \partial_{\mathbf{n}}\mu_{12}^{n+1}|_{\partial\Omega} = 0. \tag{3.33}$$

One can easily solve $(\phi_{11}, \phi_{12}, \mu_{11}, \mu_{12})^{n+1}$ from the above two sub-systems (3.31)–(3.32) since all nonlinear terms are given explicitly.

We continue to solve (3.29) in a similar way where the variable U_2^{n+1} is used to split $(\phi_2, \mu_2)^{n+1}$ into a linear combination, i.e.,

$$\phi_2^{n+1} = \phi_{21}^{n+1} + U_2^{n+1} \phi_{22}^{n+1}, \ \mu_2^{n+1} = \mu_{21}^{n+1} + U_2^{n+1} \mu_{22}^{n+1}. \tag{3.34}$$

Then the unknowns $(\phi_{21}, \phi_{22}, \mu_{21}, \mu_{22})^{n+1}$ can be obtained by solving another two subsystems that are similar to (3.31)–(3.32) with the periodic or similar boundary conditions as (3.33).

Second, we rewrite (3.19) as the following form

$$U^{n+1} = \frac{1}{2} \int_{\Omega} H^* \phi^{n+1} d\mathbf{x} + g^n, \tag{3.35}$$

where $g^n = \frac{1}{a}(bU^n - cU^{n-1}) - \frac{1}{2a} \int_{\Omega} H^*(b\phi^n - c\phi^{n-1}) d\mathbf{x}$ is an explicit form. Substituting the linear form of $(U, \phi)^{n+1}$ represented by Q^{n+1} given in (3.26) into (3.35), we get

$$U_1^{n+1} + Q^{n+1}U_2^{n+1} = \frac{1}{2} \int_{\mathcal{Q}} H^*(\phi_1^{n+1} + Q^{n+1}\phi_2^{n+1}) d\mathbf{x} + g^n. \quad (3.36)$$

Then, according to Q^{n+1} , we decompose (3.36) into the following two equalities:

$$\begin{cases} U_1^{n+1} = \frac{1}{2} \int_{\Omega} H^* \phi_1^{n+1} d\mathbf{x} + g^n, \\ U_2^{n+1} = \frac{1}{2} \int_{\Omega} H^* \phi_2^{n+1} d\mathbf{x}. \end{cases}$$
(3.37)

Substituting the linear form of $(\phi_1, \phi_2)^{n+1}$ represented by U_1^{n+1} given in (3.30) into (3.37), we get

$$\begin{cases} U_1^{n+1} = \frac{1}{2} \int_{\Omega} H^*(\phi_{11}^{n+1} + U_1^{n+1} \phi_{12}^{n+1}) d\mathbf{x} + g^n, \\ U_2^{n+1} = \frac{1}{2} \int_{\Omega} H^*(\phi_{21}^{n+1} + U_2^{n+1} \phi_{22}^{n+1}) d\mathbf{x}. \end{cases}$$
(3.38)

After applying a simple factorization to (3.38), we derive

$$U_1^{n+1} = \frac{\frac{1}{2} \int_{\Omega} H^* \phi_{11}^{n+1} d\mathbf{x} + g^n}{1 - \frac{1}{2} \int_{\Omega} H^* \phi_{12}^{n+1} d\mathbf{x}},$$
(3.39)

$$U_2^{n+1} = \frac{\frac{1}{2} \int_{\Omega} H^* \phi_{21}^{n+1} d\mathbf{x}}{1 - \frac{1}{2} \int_{\Omega} H^* \phi_{22}^{n+1} d\mathbf{x}}.$$
 (3.40)

We need verify that U_1^{n+1} and U_2^{n+1} are solvable. This can be obtained by applying a simple energy estimate to the subsystem (3.32). For any $\psi \in L^2(\Omega)$ with $\int_{\Omega} \psi d\mathbf{x} = 0$, we define $\Delta^{-1}\psi$ by

$$\Delta \phi = \psi, \int_{\mathcal{Q}} \phi d\mathbf{x} = 0. \tag{3.41}$$

Applying Δ^{-1} to the first equation of (3.32) and combining the result with the second equation of (3.32), we get

$$\frac{a}{2M\delta t}\Delta^{-1}\phi_{12}^{n+1} = (-\lambda\Delta + \frac{S}{\epsilon^2})\phi_{12}^{n+1} + H^*. \tag{3.42}$$

By taking the L^2 inner product of (3.42) with ϕ_{12}^{n+1} , we derive

$$\begin{split} &-\int_{\Omega}H^*\phi_{12}^{n+1}d\boldsymbol{x}\\ &=\frac{a}{2M\delta t}\|\nabla\Delta^{-1}\phi_{12}^{n+1}\|^2+\lambda\|\nabla\phi_{12}^{n+1}\|^2+\frac{S}{\epsilon^2}\|\phi_{12}^{n+1}\|^2\geq0. \end{split} \tag{3.43}$$

Hence, the denominator in (3.39) is non-zero, which means that U_1^{n+1} is always solvable. Similarly, U_2^{n+1} can be always solved from (3.40) as well. After calculating U_1^{n+1} and U_2^{n+1} , we further obtain ϕ_1^{n+1} , μ_1^{n+1} from (3.30), and ϕ_2^{n+1} , μ_2^{n+1} from (3.34). Third, for the velocity field $\tilde{\mathbf{u}}^{n+1}$, \mathbf{u}^{n+1} and the pressure p^{n+1}

in the scheme (3.20) and (3.22)–(3.23), we also use the nonlocal variable Q^{n+1} to split them as the following linear combinations:

$$\tilde{\mathbf{u}}^{n+1} = \tilde{\mathbf{u}}_{1}^{n+1} + Q^{n+1} \tilde{\mathbf{u}}_{2}^{n+1},
\mathbf{u}^{n+1} = \mathbf{u}_{1}^{n+1} + Q^{n+1} \mathbf{u}_{2}^{n+1}, p^{n+1} = p_{1}^{n+1} + Q^{n+1} p_{2}^{n+1}.$$
(3.44)

By replacing these variables $(\tilde{\mathbf{u}}, \mathbf{u}, p)^{n+1}$ in the scheme (3.20) and (3.22)-(3.23), and then splitting the obtained equations according to Q^{n+1} , we arrive at a system that includes two sub-equations. More precisely, from (3.20), the two split variables $\tilde{\mathbf{u}}_{i}^{n+1}$, i=1,2follow the equations:

$$\begin{cases}
\tau \frac{a}{2\delta t} \tilde{\mathbf{u}}_1^{n+1} + \alpha \tilde{\mathbf{u}}_1^{n+1} = \sigma_1, \\
\tau \frac{a}{2\delta t} \tilde{\mathbf{u}}_2^{n+1} + \alpha \tilde{\mathbf{u}}_2^{n+1} = \sigma_2,
\end{cases}$$
(3.45)

where σ_1 , σ_2 are explicit forms that are given by

$$\sigma_1 = -\nabla p^n + \tau \frac{b\mathbf{u}^n - c\mathbf{u}^{n-1}}{2\delta t}, \sigma_2 = -\phi^* \nabla \mu^*. \tag{3.46}$$

Similarly, from (3.22)–(3.23), the two split variables \mathbf{u}_i^{n+1} , p_i^{n+1} , i = 1, 2 follow the equations:

$$\begin{cases}
\tau \frac{a}{2\delta t} (\mathbf{u}_{1}^{n+1} - \tilde{\mathbf{u}}_{1}^{n+1}) + \nabla p_{1}^{n+1} = \kappa_{1}, & \nabla \cdot \mathbf{u}_{1}^{n+1} = 0, \\
\tau \frac{a}{2\delta t} (\mathbf{u}_{2}^{n+1} - \tilde{\mathbf{u}}_{2}^{n+1}) + \nabla p_{2}^{n+1} = \kappa_{2}, & \nabla \cdot \mathbf{u}_{2}^{n+1} = 0,
\end{cases} (3.47)$$

where $\kappa_1 = \nabla p^n$ and $\kappa_2 = 0$. We request the two split variables p_i^{n+1} , i = 1, 2 follow the boundary conditions described in (3.25), i.e, they are either periodic or satisfy:

$$\partial_{\mathbf{n}} p_i^{n+1}|_{\partial \Omega} = 0. \tag{3.48}$$

Fourth, we solve the auxiliary variable Q^{n+1} . Using the split form for the variables μ^{n+1} , $\tilde{\mathbf{u}}^{n+1}$, one can rewrite (3.21) as the following form:

$$\left(\frac{a}{2\delta t} - \vartheta_2\right)Q^{n+1} = \frac{1}{2\delta t}(bQ^n - cQ^{n-1}) + \vartheta_1,\tag{3.49}$$

where ϑ_i are all known from previous steps:

$$\vartheta_i = \int_{\Omega} \left(\nabla \cdot (\mathbf{u}^* \phi^*) \mu_i^{n+1} + (\phi^* \nabla \mu^*) \cdot \tilde{\mathbf{u}}_i^{n+1} \right) d\mathbf{x}, i = 1, 2. \quad (3.50)$$

We need verify that Eq. (3.49) is solvable. By taking the L^2 inner product of the second equation in (3.45) with $\tilde{\mathbf{u}}_2^{n+1}$, we obtain

$$-\int_{\Omega} (\phi^* \nabla \mu^*) \cdot \tilde{\mathbf{u}}_2^{n+1} d\mathbf{x} = (\tau \frac{a}{2\delta t} + \alpha) \|\tilde{\mathbf{u}}_{n+1}^2\|^2 \ge 0.$$
 (3.51)

By taking the L^2 inner product of the first equation in (3.29) with $M\mu_2^{n+1}$, and of the second equation in (3.29) with $-\frac{a}{2\delta t}\phi_2^{n+1}$, and then merging the two obtained equalities, we obtain

$$-\int_{\Omega} \nabla \cdot (\mathbf{u}^* \phi^*) \mu_2^{n+1} d\mathbf{x}$$

$$= \frac{a}{2\delta t} (\lambda \| \nabla \phi_2^{n+1} \|^2 + \frac{S}{\epsilon^2} \| \phi_2^{n+1} \|^2) + M \| \nabla \mu_2^{n+1} \|^2$$

$$+ \frac{a}{2\delta t} U_2^{n+1} \int_{\Omega} H^* \phi_2^{n+1} d\mathbf{x}. \tag{3.52}$$

From (3.37), it is easy to see that $U_2^{n+1}\int_{\Omega}H^*\phi_2^{n+1}d\boldsymbol{x}$ $\frac{1}{2}(\int_{\Omega}H^*\phi_2^{n+1}d\boldsymbol{x})^2\geq 0$. Thus

$$-\int_{\Omega} \nabla \cdot (\mathbf{u}^* \phi^*) \mu_2^{n+1} d\mathbf{x} \ge 0. \tag{3.53}$$

The two inequalities (3.51) and (3.53) imply $-\vartheta_2 \geq 0$ and then $\frac{a}{2\delta t} - \vartheta_2 \neq 0$, namely, (3.49) is always solvable. Finally, we update ϕ^{n+1} , μ^{n+1} , U^{n+1} from (3.26), $\tilde{\mathbf{u}}^{n+1}$, \mathbf{u}^{n+1} ,

and p^{n+1} from (3.44).

In summary, we implement the scheme (3.17)–(3.23) in the following way:

- Step 1: Compute $(\phi_{ij}, \mu_{ij})^{n+1}$, i, j = 1, 2 from (3.31)–(3.32) and another similar two subsystems split from (3.29) using the variable U_2^{n+1} ;
- Step 2: Update U_1^{n+1} , U_2^{n+1} from (3.39) and (3.40);
- Step 3: Update $(\phi_i, \mu_i)^{n+1}$, i = 1, 2 from (3.30) and (3.34); Step 4: Compute $\tilde{\mathbf{u}}_i^{n+1}$, i = 1, 2 from (3.45);
- Step 5: Compute \mathbf{u}_{i}^{n+1} and p_{i}^{n+1} , i = 1, 2 from (3.47);
- Step 6: Compute Q^{n+1} from (3.49);
- Step 7: Update ϕ^{n+1} , μ^{n+1} , U^{n+1} from (3.26), $\tilde{\mathbf{u}}^{n+1}$, \mathbf{u}^{n+1} , and p^{n+1} from (3.44).

Remark 3.5. For step 5, by applying the divergence operator ∇ . to (3.47) and using the divergence-free conditions for \mathbf{u}_i^{n+1} , we can obtain the following Poisson equation for p_i^{n+1} with the periodic boundary conditions or homogeneous Neumann boundary conditions, i.e.,

$$-\Delta p_i^{n+1} = -\frac{a\tau}{2\delta t} \nabla \cdot \tilde{\mathbf{u}}_i^{n+1} - \nabla \cdot \kappa_i. \tag{3.54}$$

Once p_i^{n+1} is computed from (3.54), we update \mathbf{u}_i^{n+1} by using

$$\mathbf{u}_{i}^{n+1} = \tilde{\mathbf{u}}_{i}^{n+1} - \frac{2\delta t}{a\tau} \nabla p_{i}^{n+1} + \frac{2\delta t}{a\tau} \kappa_{i}. \tag{3.55}$$

Hence, the total computational cost needed by the scheme (3.17)–(3.23) at each time step includes solving four independent elliptic linear systems in Step 1 and two Poisson-type equations in Step 5. All these equations have constant coefficients and are fully-decoupled, which means very efficient calculations in practice.

The following theorem ensures that the developed scheme (3.17)–(3.23) satisfies the energy stability unconditionally.

Theorem 3.1. The following discrete energy dissipation law holds for the scheme (3.17)–(3.23),

$$\frac{1}{\delta t} (E^{n+1} - E^n) \le -\alpha \|\tilde{\mathbf{u}}^{n+1}\|^2 - M \|\nabla \mu^{n+1}\|^2 \le 0, \tag{3.56}$$

where

$$\begin{split} E^{n+1} &= \frac{\tau}{2} \left(\frac{1}{2} \| \mathbf{u}^{n+1} \|^2 + \frac{1}{2} \| 2 \mathbf{u}^{n+1} - \mathbf{u}^n \|^2 \right) \\ &+ \frac{\lambda}{2} \left(\frac{1}{2} \| \nabla \phi^{n+1} \|^2 + \frac{1}{2} \| 2 \nabla \phi^{n+1} - \nabla \phi^n \|^2 \right) \\ &+ \lambda \left(\frac{1}{2} |U^{n+1}|^2 + \frac{1}{2} |2U^{n+1} - U^n|^2 \right) \\ &+ \frac{1}{2} \left(\frac{1}{2} |Q^{n+1}|^2 + \frac{1}{2} |2Q^{n+1} - Q^n|^2 \right) \\ &+ \frac{\delta t^2}{3\tau} \| \nabla p^{n+1} \|^2 + \frac{\lambda S}{2\epsilon^2} \| \phi^{n+1} - \phi^n \|^2. \end{split} \tag{3.57}$$

Proof. We multiply the inner product of (3.20) with $2\delta t \tilde{\mathbf{u}}^{n+1}$ in the L^2 space to get

$$\tau(3\tilde{\mathbf{u}}^{n+1} - 4\mathbf{u}^n + \mathbf{u}^{n-1}, \tilde{\mathbf{u}}^{n+1}) + 2\alpha\delta t \|\tilde{\mathbf{u}}^{n+1}\|^2$$

$$+ 2\delta t(\nabla p^n, \tilde{\mathbf{u}}^{n+1}) + 2\delta t Q^{n+1} \int_{\Omega} \phi^* \nabla \mu^* \cdot \tilde{\mathbf{u}}^{n+1} d\mathbf{x} = 0.$$
 (3.58)

From (3.22), for any variable \mathbf{v} with $\nabla \cdot \mathbf{v} = 0$, we have

$$(\mathbf{u}^{n+1}, \mathbf{v}) = (\tilde{\mathbf{u}}^{n+1}, \mathbf{v}). \tag{3.59}$$

We derive following equality

$$\tau(3\tilde{\mathbf{u}}^{n+1} - 4\mathbf{u}^{n} + \mathbf{u}^{n-1}, \tilde{\mathbf{u}}^{n+1})
= \tau(3\tilde{\mathbf{u}}^{n+1} - 4\mathbf{u}^{n} + \mathbf{u}^{n-1}, \mathbf{u}^{n+1})
+ \tau(3\tilde{\mathbf{u}}^{n+1} - 4\mathbf{u}^{n} + \mathbf{u}^{n-1}, \tilde{\mathbf{u}}^{n+1} - \mathbf{u}^{n+1})
= \tau(3\mathbf{u}^{n+1} - 4\mathbf{u}^{n} + \mathbf{u}^{n-1}, \mathbf{u}^{n+1})
+ \tau(3\tilde{\mathbf{u}}^{n+1}, \tilde{\mathbf{u}}^{n+1} - \mathbf{u}^{n+1})
= \tau(3\mathbf{u}^{n+1} - 4\mathbf{u}^{n} + \mathbf{u}^{n-1}, \mathbf{u}^{n+1})
+ 3\tau(\tilde{\mathbf{u}}^{n+1} - \mathbf{u}^{n+1}, \tilde{\mathbf{u}}^{n+1} + \mathbf{u}^{n+1})
= \frac{\tau}{2} \Big(\|\mathbf{u}^{n+1}\|^{2} - \|\mathbf{u}^{n}\|^{2} + \|2\mathbf{u}^{n+1} - \mathbf{u}^{n}\|^{2} - \|2\mathbf{u}^{n} - \mathbf{u}^{n-1}\|^{2}
+ \|\mathbf{u}^{n+1} - 2\mathbf{u}^{n} + \mathbf{u}^{n-1}\|^{2} \Big) + 3\tau(\|\tilde{\mathbf{u}}^{n+1}\|^{2} - \|\mathbf{u}^{n+1}\|^{2}),$$
(3.60)

where we use the following identity

$$2(3a - 4b + c, a)$$

$$= a^{2} - b^{2} + (2a - b)^{2} - (2b - c)^{2} + (a - 2b + c)^{2}.$$
(3.61)

We reformulate the projection step (3.22) as

$$\frac{3\tau}{2\delta t}\mathbf{u}^{n+1} + \nabla p^{n+1} = \frac{3\tau}{2\delta t}\tilde{\mathbf{u}}^{n+1} + \nabla p^{n}.$$
 (3.62)

By taking the square of both sides of the above equation, we get

$$\frac{9\tau^{2}}{4\delta t^{2}} \|\mathbf{u}^{n+1}\|^{2} + \|\nabla p^{n+1}\|^{2}
= \frac{9\tau^{2}}{4\delta t^{2}} \|\tilde{\mathbf{u}}^{n+1}\|^{2} + \|\nabla p^{n}\|^{2} + \frac{3\tau}{\delta t} (\tilde{\mathbf{u}}^{n+1}, \nabla p^{n}).$$
(3.63)

Hence, by multiplying $\frac{2\delta t^2}{3\tau}$ of the above equation, we derive

$$\frac{3\tau}{2}(\|\mathbf{u}^{n+1}\|^2 - \|\tilde{\mathbf{u}}^{n+1}\|^2) + \frac{2\delta t^2}{3\tau}(\|\nabla p^{n+1}\|^2 - \|\nabla p^n\|^2)
= 2\delta t(\tilde{\mathbf{u}}^{n+1}, \nabla p^n).$$
(3.64)

By taking the inner product of (3.22) with $2\tau \delta t \mathbf{u}^{n+1}$ in the L^2 space, we have

$$\frac{3\tau}{2}(\|\mathbf{u}^{n+1}\|^2 - \|\tilde{\mathbf{u}}^{n+1}\|^2 + \|\mathbf{u}^{n+1} - \tilde{\mathbf{u}}^{n+1}\|^2) = 0.$$
 (3.65)

We combine (3.58), (3.60), (3.64), and (3.65) to obtain

$$\frac{\tau}{2}(\|\mathbf{u}^{n+1}\|^{2} - \|\mathbf{u}^{n}\|^{2} + \|2\mathbf{u}^{n+1} - \mathbf{u}^{n}\|^{2} - \|2\mathbf{u}^{n} - \mathbf{u}^{n-1}\|^{2}
+ \|\mathbf{u}^{n+1} - 2\mathbf{u}^{n} + \mathbf{u}^{n-1}\|^{2})
+ \frac{3\tau}{2}\|\mathbf{u}^{n+1} - \tilde{\mathbf{u}}^{n+1}\|^{2}
+ \frac{2\delta t^{2}}{3\tau}(\|\nabla p^{n+1}\|^{2} - \|\nabla p^{n}\|^{2}) + 2\alpha\delta t\|\tilde{\mathbf{u}}^{n+1}\|^{2}
+ 2\delta tQ^{n+1} \int_{\Omega} (\phi^{*}\nabla \mu^{*}) \cdot \tilde{\mathbf{u}}^{n+1} d\mathbf{x} = 0.$$
(3.66)

Computing the inner product of (3.17) with $2\delta t \mu^{n+1}$ in the L^2 space, we have

$$(3\phi^{n+1} - 4\phi^n + \phi^{n-1}, \mu^{n+1})$$

$$+ 2\delta t Q^{n+1} \int_{\Omega} \nabla \cdot (\mathbf{u}^* \phi^*) \mu^{n+1} d\mathbf{x} + 2\delta t M \|\nabla \mu^{n+1}\|^2 = 0.$$
(3.67)

Computing the L^2 inner product of (3.18) with $-(3\phi^{n+1}-4\phi^n+\phi^{n-1})$, we find

$$-(\mu^{n+1}, 3\phi^{n+1} - 4\phi^{n} + \phi^{n-1})$$

$$+ \lambda(\nabla\phi^{n+1}, \nabla(3\phi^{n+1} - 4\phi^{n} + \phi^{n-1}))$$

$$+ \lambda U^{n+1} \int_{\Omega} H^{*}(3\phi^{n+1} - 4\phi^{n} + \phi^{n-1}) d\mathbf{x}$$

$$+ \lambda \frac{S}{c^{2}}(\phi^{n+1} - \phi^{*}, 3\phi^{n+1} - 4\phi^{n} + \phi^{n-1}) = 0.$$
(3.68)

By multiplying (3.19) with $2\lambda U^{n+1}$ and using (3.61) we obtain

$$\lambda \left(|U^{n+1}|^2 - |U^n|^2 + |2U^{n+1} - U^n|^2 - |2U^n - U^{n-1}|^2 + |U^{n+1} - 2U^n + U^{n-1}|^2 \right)$$

$$= \lambda U^{n+1} \int_{\Omega} H^* (3\phi^{n+1} - 4\phi^n + \phi^{n-1}) d\mathbf{x}.$$
(3.69)

By multiplying (3.21) with $2\delta tQ^{n+1}$ and using (3.61) we obtain

$$\frac{1}{2} \left(|Q^{n+1}|^2 - |Q^n|^2 + |2Q^{n+1} - Q^n|^2 - |2Q^n - Q^{n-1}|^2 + |Q^{n+1} - 2Q^n + Q^{n-1}|^2 \right)
+ 2\delta t Q^{n+1} \int_{\Omega} \left(\nabla \cdot (\mathbf{u}^* \phi^*) \mu^{n+1} + (\phi^* \nabla \mu^*) \cdot \tilde{\mathbf{u}}^{n+1} \right) d\mathbf{x}.$$
(3.70)

Hence, by combining (3.66)–(3.70), we arrive at
$$\frac{\tau}{2}(\|\mathbf{u}^{n+1}\|^2 - \|\mathbf{u}^n\|^2 + \|2\mathbf{u}^{n+1} - \mathbf{u}^n\|^2 - \|2\mathbf{u}^n - \mathbf{u}^{n-1}\|^2)$$

$$+ \frac{2\delta t^2}{3\tau}(\|\nabla p^{n+1}\|^2 - \|\nabla p^n\|^2)$$

$$+ \frac{\lambda}{2}(\|\nabla \phi^{n+1}\|^2 - \|\nabla \phi^n\|^2 + \|\nabla(2\phi^{n+1} - \phi^n)\|^2$$

$$- \|\nabla(2\phi^n - \phi^{n-1})\|^2)$$

$$+ \lambda(\|U^{n+1}\|^2 - |U^n|^2 + |2U^{n+1} - U^n|^2 - |2U^n - U^{n-1}|^2)$$

$$+ \frac{1}{2}(\|Q^{n+1}\|^2 - |Q^n|^2 + |2Q^{n+1} - Q^n|^2 - |2Q^n - Q^{n-1}|^2)$$

$$+ \frac{\lambda S}{\epsilon^2}(\|\phi^{n+1} - \phi^n\|^2 - \|\phi^n - \phi^{n-1}\|^2)$$

$$+ \left\{\frac{\tau}{2}\|\mathbf{u}^{n+1} - 2\mathbf{u}^n + \mathbf{u}^{n-1}\|^2 + \frac{3\tau}{2}\|\mathbf{u}^{n+1} - \tilde{\mathbf{u}}^{n+1}\|^2$$

$$+ \frac{\lambda}{2}\|\nabla(\phi^{n+1} - 2\phi^n + \phi^{n-1})\|^2 + \frac{2\lambda S}{\epsilon^2}\|\phi^{n+1} - 2\phi^n + \phi^{n-1}\|^2$$

$$+ \lambda |U^{n+1} - 2U^n + U^{n-1}|^2 + \frac{1}{2}|Q^{n+1} - 2Q^n + Q^{n-1}|^2\right\}$$

$$= -2\delta t\alpha \|\tilde{\mathbf{u}}^{n+1}\|^2 - 2\delta tM \|\nabla \mu^{n+1}\|^2,$$
(3.71)

where we use the following identity:

$$(3a-4b+c)(a-2b+c) = (a-b)^2 - (b-c)^2 + 2(a-2b+c)^2. (3.72)$$

Finally, we obtain (3.56) from (3.71) after dropping the positive terms in $\{ \}$. \Box

4. Numerical simulation

In this section, we first implement several numerical examples to verify the energy stability and convergence rate of the proposed scheme (3.17)–(3.23). Then we perform several benchmark simulations including the spinodal decompositions in 2D and 3D and fingering instability in 2D and 3D, to show the effectiveness of the scheme. In all the examples below, the computed domain is set to a rectangle or a rectangular body. For directions with periodic boundary conditions, we use the Fourier-spectral method to perform the discretization. For the directions with boundary conditions specified in (3.25), we use the spectral Legendre–Galerkin method to perform the discretization.

4.1. Stability tests

In this subsection, we perform several stability tests in 2D to verify the unconditional energy stability of the fully-decoupled scheme (3.17)–(3.23). The initial conditions at $t=t^0$ for all variables are set as follows (as shown in the first subfigure of Fig. 4.3),

$$\begin{cases} \phi^{0}(x, y) = 1 + \sum_{i=1}^{2} \tanh(\frac{r_{i} - \sqrt{(x - x_{i})^{2} + (y - y_{i})^{2}}}{1.5\epsilon}), \\ \mathbf{u}^{0}(x, y) = \mathbf{0}, p^{0}(x, y) = 0, \end{cases}$$
(4.1)

where $r_1 = 1.4$, $r_2 = 0.5$, $x_1 = \pi - 0.8$, $x_2 = \pi + 1.7$, $y_1 = y_2 = \pi$. The computational domain is $\Omega = [0, 2\pi]^2$ and the periodic boundary conditions are assumed. We use the Fourier-spectral method and 128 Fourier modes for each direction to discretize the space such that the interface is resolved well by sufficiently fine mesh. The parameters read as

$$\tau = 1, \alpha = 100, M = 1, \epsilon = 5e-2, \lambda = 0.01, B = 10, S = 2.$$
(4.2)

Note that the scheme (3.17)–(3.23) contains an additional stabilizer (term S in (3.18)), to verify whether it effectively enhances the stability, we compare the numerical solutions obtained by the stabilized version ($S \neq 0$) with that obtained by using the non-stabilized version (S = 0). For convenience, we use DSAV to denote the stabilized version ((3.17)–(3.23) with S = 2), and SAV to denote the non-stabilized version ((3.17)–(3.23) with S = 0).

In Figs. 4.1 and 4.2, we compute the original free energy (2.14) and the modified free energy (3.57) computed by using different time steps to verify the energy stability of DSAV and SAV.

- First, we plot the energy evolution curves calculated using SAV with a time step of $\delta t = 0.01$. It can be seen from Fig. 4.1(a) that the modified energy of the system (3.57) does show a monotonic downward trend, while the original energy (2.14) shows an upward trend. Moreover, the difference between the two energies is very large. We again use a smaller time step of $\delta t = 0.01/2^7$, but the results obtained have not improved, as shown in Fig. 4.1(b).
- Then, we use the scheme DSAV and different time steps to plot the original energy evolution curves in Fig. 4.2 (a). The results show that the obtained energy curves present a good monotonic attenuation, which means that the stabilizer S can effectively stabilize the computations. In Fig. 4.2 (b), we use SAV and time step $\delta t = 0.01/2^8$ to plot the time evolution of the original energy (2.14) and compare it with the result obtained by using DSAV with the time step $\delta t = 0.01/2^4$. We find that the two energy curves are very consistent. However, the time step of $0.01/2^8$ is the maximum time step size that can be used by SAV to get the decaying energy evolution curve. This means that if the expected energy curves are the same, the time step available in DSAV is 32 times the time step available in SAV.
- Finally, we use DSAV and time step $\delta t = 0.01/2^4$ to run to the steady-state. Fig. 4.3 shows the profiles of ϕ at different times. It can be seen that due to the coarsening effect, the small circle is gradually absorbed by the large circle. In Fig. 4.4(a), we plot the evolution curve of the original energy (2.14) and the modified energy (3.57) with the time that are computed from DSAV and time step $\delta t = 0.01/2^4$. We find that the difference between these two energies is very small. Also, in Fig. 4.4(b), we plot the evolution of the value of the auxiliary variable Q over time using different time steps. We find that as the time step size gradually decreases, the size of Q tends to 1, which means that if the time step is small, the two integral terms in (3.21) will be closer to 0.

4.2. Accuracy tests

In this subsection, we perform convergence tests to verify the accuracy of the scheme DSAV. For comparisons, we also compute the numerical solutions by using the following schemes:

- DSAV scheme but no Q and no S (by setting $Q^n \equiv 1$ for any n such that (3.21) is removed, and setting S = 0 in the scheme (3.17)–(3.23) to illustrate the effectiveness of additional stabilizer S), referred to as AV;
- DSAV scheme with S but no Q (by setting $Q^n \equiv 1$ for any n such that (3.21) is removed), i.e., the advection and surface tension terms are all treated explicitly, referred to as EX-SAV;
- ullet Convex-splitting scheme (the scheme developed in [28] where the nonlinear term $f(\phi)$ is discretized using the second-order convex-splitting approach, and the advection and surface tension terms are treated by implicit–explicit combinations), referred to as CS.

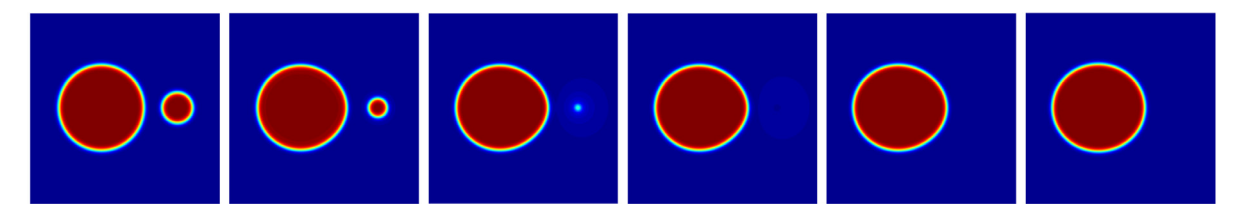
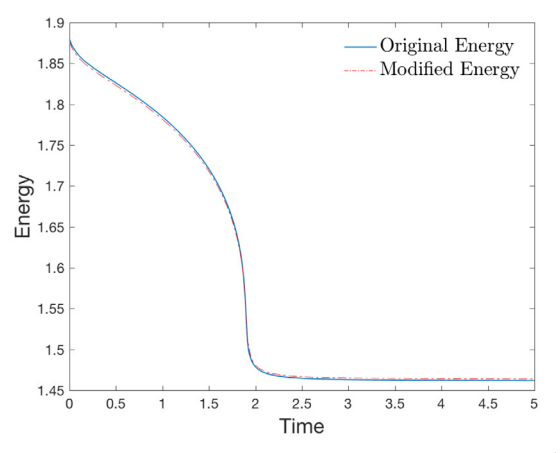
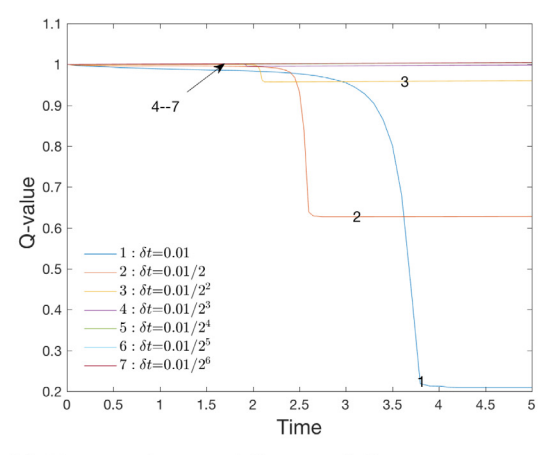


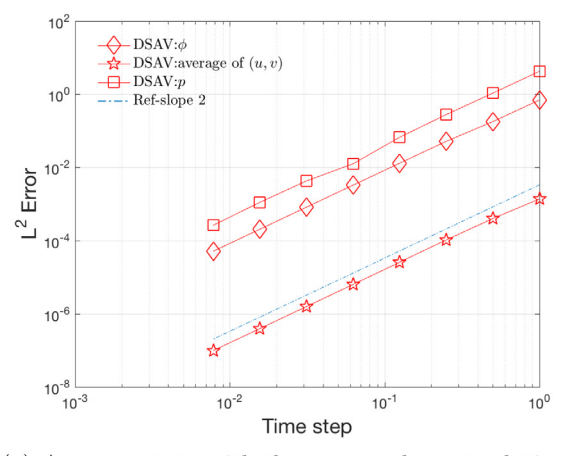
Fig. 4.3. The profiles of ϕ computed using the scheme DSAV with time step $\delta t = 0.01/2^4$. Snapshots are taken at t = 0, 1.4, 1.9, 1.95, 2.45, and 5, where the initial conditions are given in (4.1).

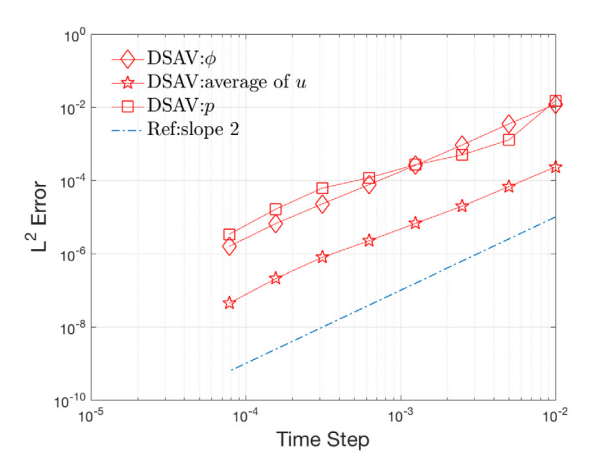




- (a) Original and modified energy with $\delta t = 0.01/2^4$.
- (b) Time evolution of Q using different time steps.

Fig. 4.4. (a) The evolution of the original energy (2.14) and modified energy (3.57) calculated by DSAV using the time step $\delta t = 0.01/2^4$. (b) The evolution of the auxiliary variable Q computed by using different time steps.





- (a) Accuracy tests with the presumed exact solutions.
- (b) Accuracy tests by refinement in time step.

Fig. 4.5. (a) Convergence tests by using the pre-assumed exact solutions given in (4.3) where L^2 numerical errors of ϕ , the average of $\mathbf{u} = (u, v)$, and p are computed by DSAV using different time steps at t = 10. (b) Convergence tests by refinement in time step calculated by DSAV with the initial conditions given in (4.1) and different time steps.

We first perform convergence tests by assuming the exact solutions of the system (2.3)–(2.6) are known, which are given by

$$\phi(x, y, t) = \sin x \cos y \cos t, p(x, y, t) = \sin x \sin y \sin t,$$

$$u(x, y, t) = \cos x \sin y \cos t, v(x, y, t) = -\sin x \cos y \cos t,$$
(4.3)

and apply some suitable force fields so that the given solutions in (4.3) satisfy the system. We set the 2D computational domain

as
$$\Omega = [0, 2\pi]^2$$
, and set the model parameters as $\tau = 1, \alpha = 100, M = 1, \epsilon = 0.1, \lambda = 0.01, B = 10, S = 2.$ (4.4)

We assume the periodic boundary conditions and use 128 Fourier modes to discretize each direction. Therefore, compared to the time discretization error, the spatial discretization error is negligible. In Fig. 4.5 (a), we plot the numerical errors of L^2 at t=10 of the all unknown variables between the obtained numerical solution and the given exact solution (4.3) by using different time

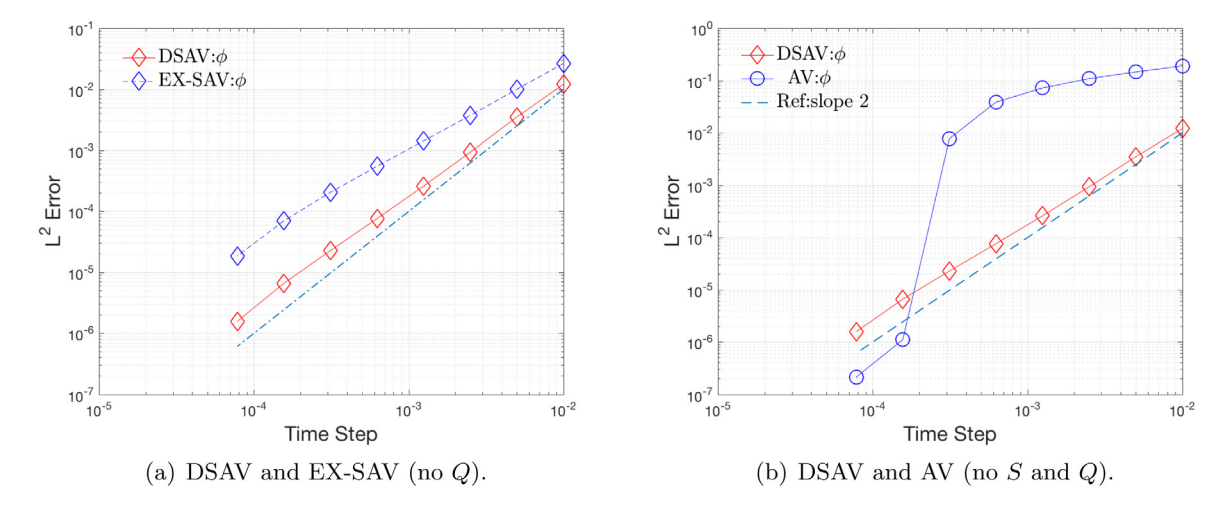


Fig. 4.6. Convergence tests by refinement in the time step, where (a) the L^2 numerical errors of ϕ computed by using the schemes DSAV and EX-SAV (no Q) with different time steps, and (b) the L^2 numerical errors of ϕ computed by using the schemes DSAV and SAV (no S and Q) with different time steps.

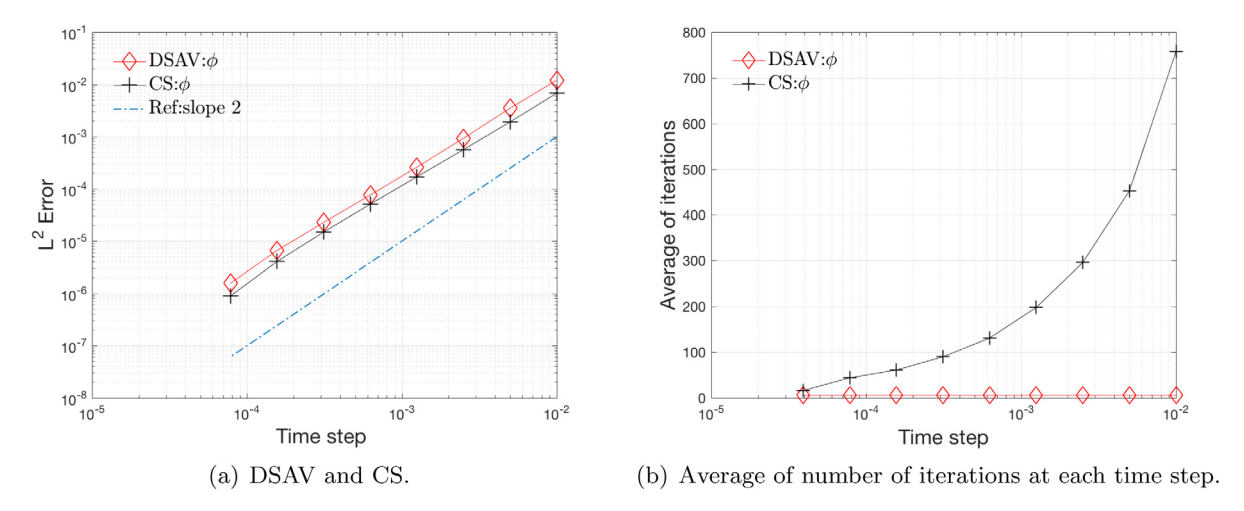


Fig. 4.7. Convergence tests by refinement in the time step, where (a) the L^2 numerical errors of ϕ computed by using the schemes DSAV and CS with different time steps; and (b) the average number of iterations required by the two schemes at each time step. (Note: DSAV does not require any iterations at each time step, but it requires solving six linear equations with constant coefficients, thus we count the number of iterations as 6.)

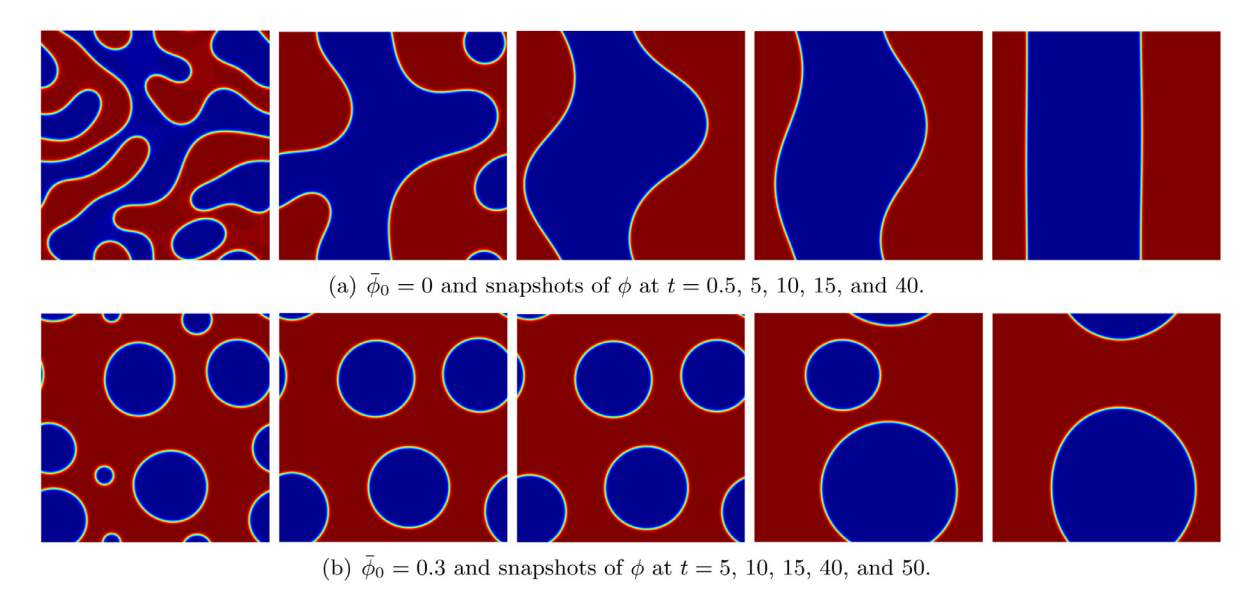


Fig. 4.8. 2D dynamics of spinodal decomposition examples computed using the scheme DSAV. Snapshots of ϕ are taken at different times, where the initial conditions are (a) $\bar{\phi}_0 = 0$ and (b) $\bar{\phi}_0 = 0.3$.

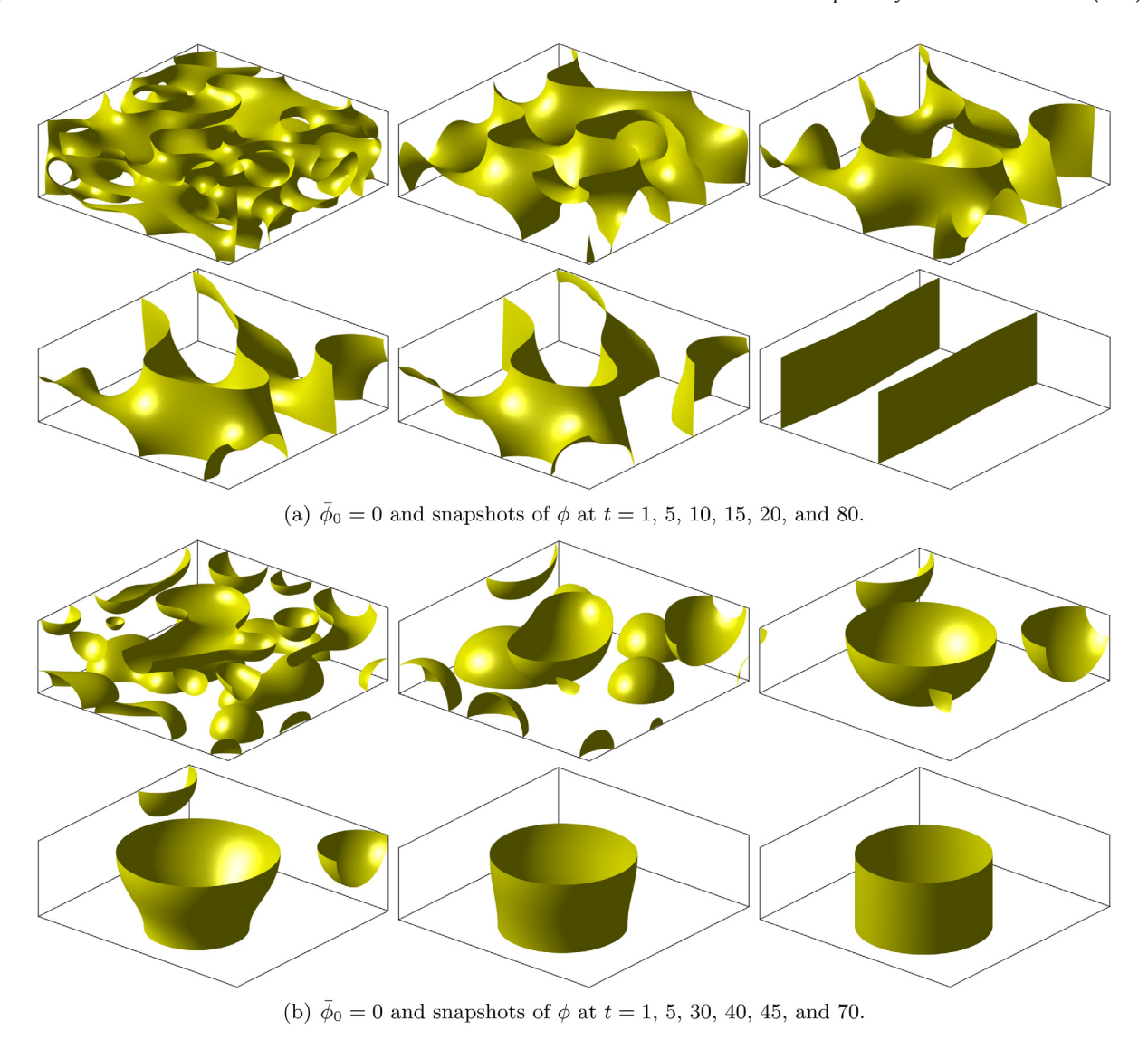


Fig. 4.9. 3D dynamics of spinodal decomposition examples computed using the scheme DSAV. Snapshots of the isosurfaces $\{\phi=0\}$ are plotted at different times, where the initial conditions are (a) $\bar{\phi}_0=0$ and (b) $\bar{\phi}_0=0.5$.

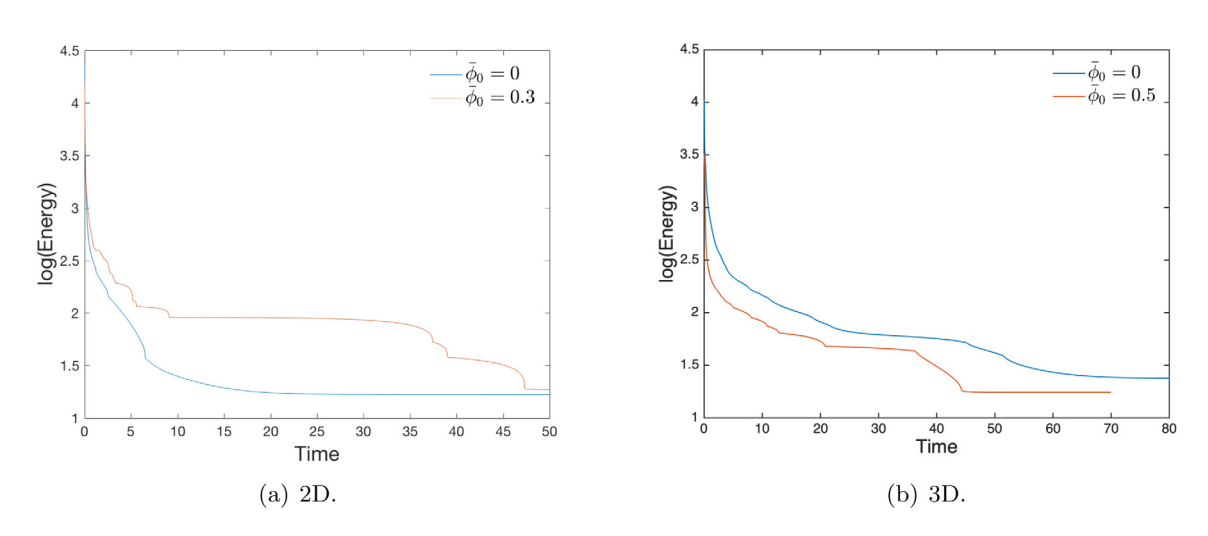


Fig. 4.10. The evolution over time of the logarithm of the total free energy (3.57) calculated by DSAV for all 2D and 3D spinodal decompositions in (a) 2D and (b) 3D.

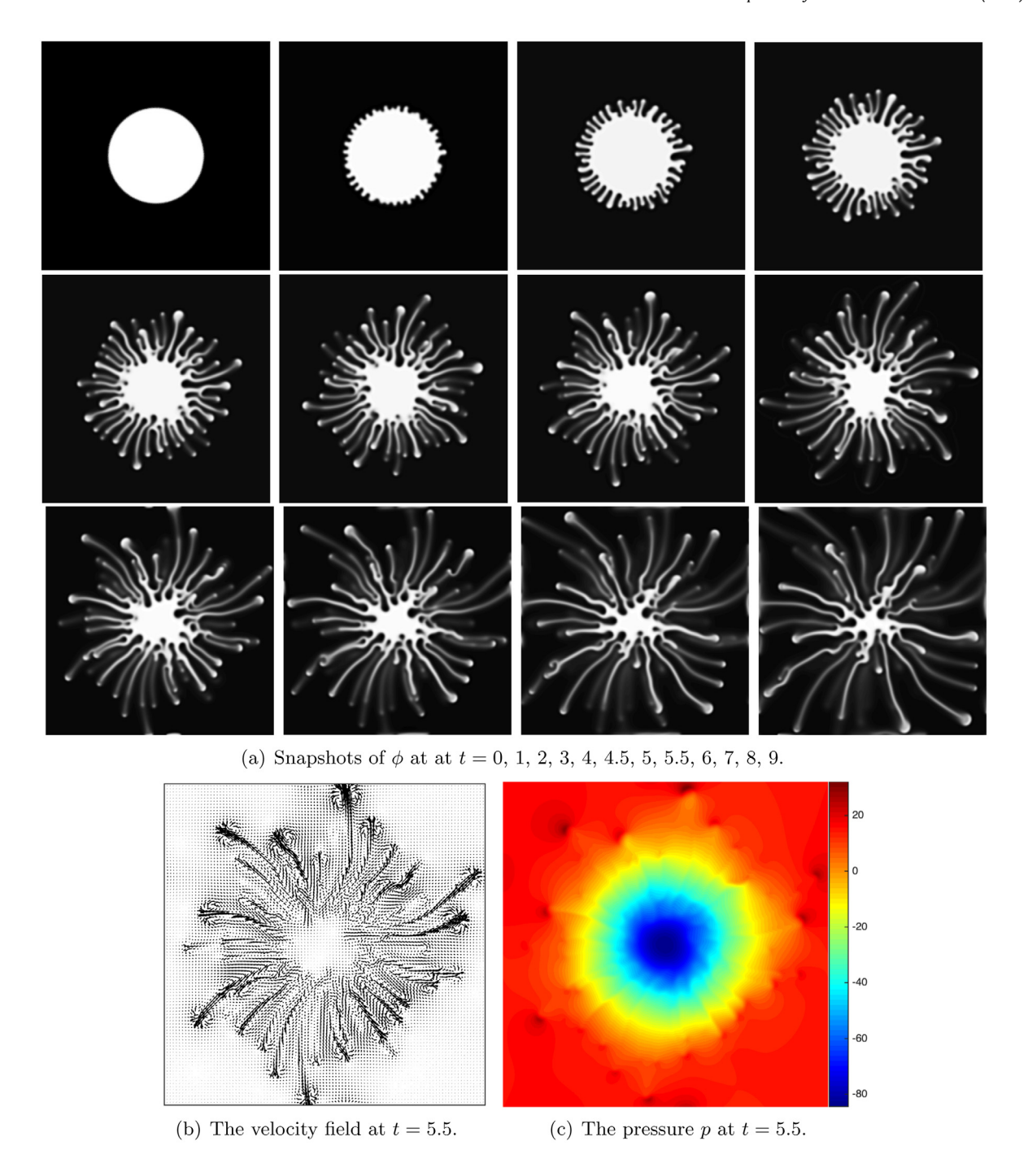


Fig. 4.11. (a) 2D fingering pattern example where snapshots of ϕ are taken at various times, (b) the velocity field at t=5.5, and (c) the pressure p at t=5.5.



Fig. 4.12. Comparison of number of fingers where $\lambda=0.01,\,0.001,\,0.0005,\,0.0001,\,$ and 0.00001, from left to right.

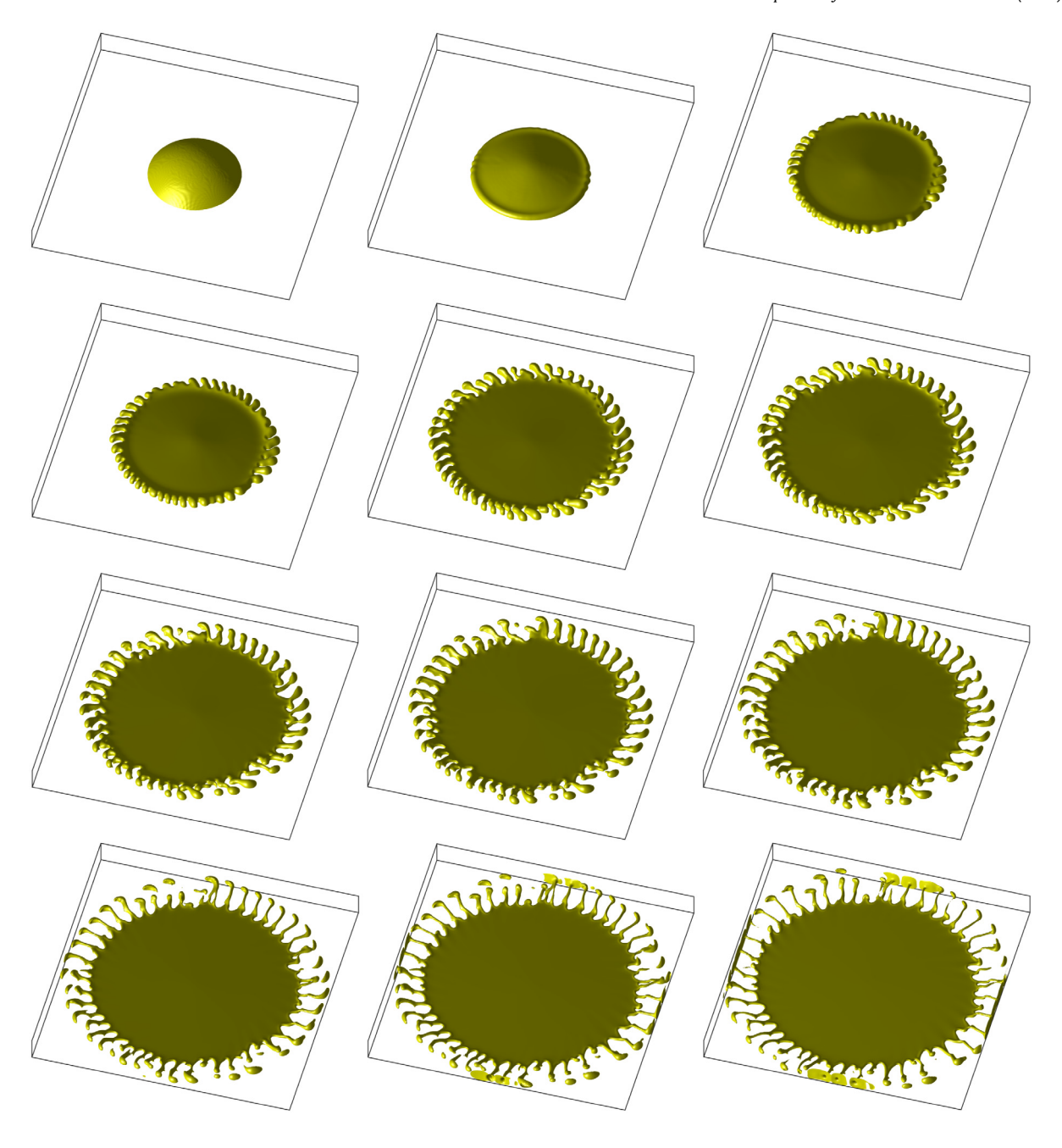


Fig. 4.13. 3D fingering pattern example where snapshots of isosurfaces $\{\phi = 0\}$ are taken at t = 0, 0.4, 0.8, 0.9, 1.2, 1.3, 1.4, 1.5, 1.6, 1.7, 1.8, and 1.9.

steps. We note that the scheme DSAV provides almost perfect second-order accuracy for all variables.

We further test the convergence rates by performing mesh refinement in time. We use the initial conditions given in (4.1) and the model parameters given in (4.2). Since the exact solutions are not known yet, we choose the numerical solutions computed by the scheme DSAV with a very tiny time step size $\delta t=1\mathrm{e}{-9}$ as the exact solution.

• In Fig. 4.5 (b), we plot the L^2 errors of ϕ computed by DSAV between the numerical solution and the exact solution at t=0.2 where the time step δt is changed from $\delta t=0.01$ to $\delta t=\frac{0.01}{2^7}$ with a factor of 1/2. The computed results show the expected second-order of accuracy for all variables.

- In Fig. 4.6(a), we compare the convergence rate obtained by using schemes DSAV and EX-SAV (DSAV but no Q). We observe that both schemes exhibit a second-order convergence rate. But for any fixed time step δt , the magnitude of the error calculated using the scheme DSAV is much smaller than the error calculated using the scheme EX-SAV. This means that the scheme DSAV is more accurate because the second auxiliary variable Q records all variances caused by the coupled nonlinear terms.
- In Fig. 4.6 (b), we plot the L^2 errors of ϕ by using the schemes DSAV and AV (DSAV but no S and Q) by refining the time step. We observe that the scheme DSAV always presents almost perfect second-order accuracy. However, when AV uses a large time step of $\delta t > 0.01/2^6$, the convergence

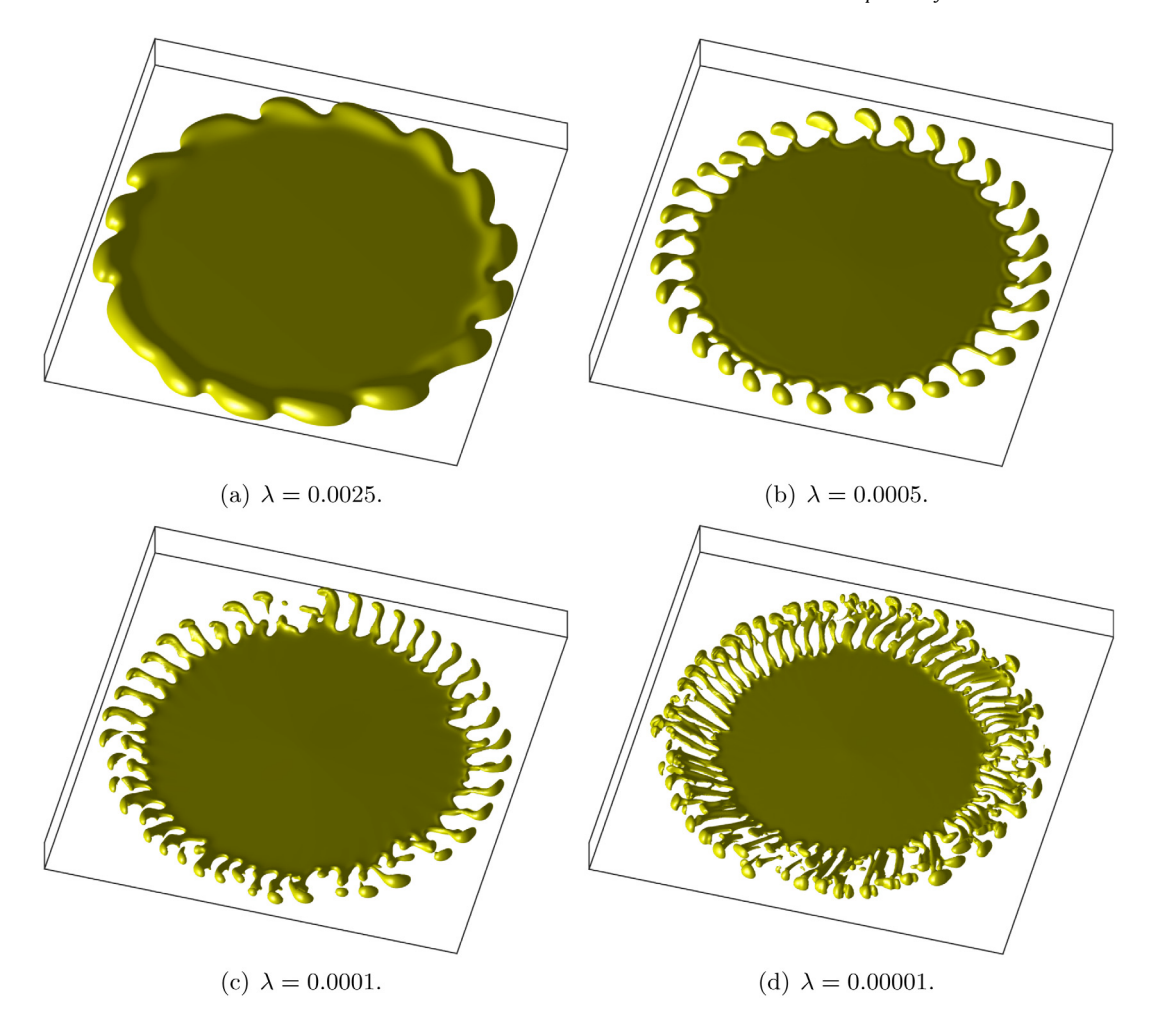


Fig. 4.14. Comparison of number of 3D fingers where $\lambda = 0.0025$, 0.0005, 0.0001, and 0.00001.

rate is very poor. Only when a smaller time step is used $(\delta t \le 0.01/2^7)$, AV can display second-order accuracy.

• In Fig. 4.7 (a), we compare the error of ϕ calculated by DSAV and CS. Both schemes present the second-order convergence rate. We note that for any fixed time step δt , the magnitude of the error calculated using CS is slightly smaller than the error calculated using DSAV because of its implicit processing for the nonlinear term. But in Fig. 4.7 (b), we also compare the number of iterations required for each time step. Although DSAV does not require iterations at each time step, it needs solving six elliptic equations, so we still count the number of iterations as 6. We can see that the scheme CS requires a large number of iterations and is very time-consuming. For example, when $\delta t = 0.01$, CS needs around 800 iterations per step. This means that CS requires a lot of CPU time, which reflects the effectiveness of DSAV.

4.3. Spinodal decomposition in 2D and 3D

In this example, we use the developed scheme DSAV to study the spinodal decomposition (phase separation). By setting the initial condition to a uniform binary mixture with a certain range of random number perturbations, the system can evolve from a uniform state to the two-phase state, which is caused by the spontaneous growth of the concentration fluctuations.

We give the initial conditions as follows,

$$\mathbf{u}^{0}(\mathbf{x}) = 0, p^{0}(\mathbf{x}) = 0, \phi(\mathbf{x}) = \bar{\phi}_{0} + 0.001 \text{rand}(\mathbf{x}),$$
 (4.5)

where the rand(x) is the random number in [-1, 1] that follows the normal distribution.

We first perform 2D simulations. The computational domain is $\Omega=[0,2\pi]^2$ that is equipped with the periodic boundary conditions. We use the Fourier-spectral method to discretize the space, and use 512 Fourier mode for each direction. The model parameters are set as $\tau=1$, $\alpha=100$, M=1, $\epsilon=0.025$, B=10, S=10, $\lambda=0.01$, and the time step is set as $\delta t=1$ e-3. In Fig. 4.8, two simulations with initial average $\bar{\phi}_0=0$ and $\bar{\phi}_0=0.3$ are performed. Snapshots of the profiles of ϕ at various times are plotted in Fig. 4.8 (a)–(b). We find that the final equilibrium solutions in the two simulations show a banded phase and a circular phase, respectively.

We then perform 3D simulations. The computational domain to be $\Omega=[0,2\pi]\times[0,2\pi]\times[0,2]$. The periodic boundary conditions are assumed for x- and y-directions which are then discretized by using the Fourier-spectral method with 256 Fourier modes for each direction. The boundary conditions along the z-direction read as $(p_z,\phi_z,\mu_z)|_{(z=0,2)}=0$ and the spatial discretization for z-direction is discretized by using the Legendre-Galerkin method and the Legendre polynomials with degrees up to 256. We set the initial average value $\bar{\phi}_0=0$ and $\bar{\phi}_0=0.5$, and plot the dynamical evolutions of the isosurface $\{\phi=0\}$ at

different times in Fig. 4.9 (a)–(b). We observe that the equilibrium solution presents the lamella phase when $\bar{\phi}_0=0$, and the cylindrical phase when $\bar{\phi}_0=0.5$.

In Fig. 4.10, we present the time evolution of the total free energy functional (3.57) for all 2D and 3D simulations. The energy curves show the decay over time, which confirms that the developed algorithm is unconditionally stable.

4.4. Fingering pattern in 2D and 3D

When a liquid droplet is located in the rotating Hele–Shaw cell, the rotating motion will cause the fluid interface to become centrifugally unstable and deformed. In the experiment, a rich swirling fingering pattern was observed, for example, they may change from teardrop-like structures to filament-like arms with extended ends, or branched skeleton structures with almost constant fingertip width, see [51–55]. In this section, we investigate the fingering pattern instability by imposing the rotating force in the Darcy equations, where the momentum equation (2.5) is replaced by the following form:

$$\tau \mathbf{u}_t + \alpha \mathbf{u} + \nabla p + \phi \nabla \mu = g \frac{(1+\phi)}{2} (\omega^2 \mathbf{r} + 2\omega (e_z \times \mathbf{u})). \tag{4.6}$$

where $e_z = (0, 0, 1)$.

We first perform a 2D simulation with the computed domain $\Omega = [0, 2\pi]^2$. The initial conditions read as follows:

$$\phi^{0} = \tanh(\frac{r_{0} - \sqrt{(x - \pi)^{2} - (y - \pi)^{2}}}{\epsilon}), \mathbf{u}^{0} = (0, 0), p^{0} = 0,$$
(4.7)

where $r_0 = 1.3 + 0.01 \text{rand}(\textbf{x})$ where rand(x) is the random number in [0, 1]. For simplicity, we assume periodic boundary conditions and discretize the space by using the Fourier-spectral method, where each direction is discretized using 2048 Fourier modes. The model parameters read as

$$\tau = 1, \alpha = 40, M = 0.01, \epsilon = 0.0125, \lambda = 0.0001, B = 10,$$

 $S = 2, \omega = 5, g = 5, \mathbf{r} = (x - \pi, y - \pi).$ (4.8)

In Fig. 4.11 (a), snapshots of the phase-field variable ϕ at different times are plotted using the black-white color map. We observe that a large number of fingers are formed over time. In Fig. 4.11 (b) and (c), we plot the velocity field and the pressure p at t=5.5. It can be seen that the velocity field presents a clear vortex in the vicinity of each finger. In Fig. 4.12, by using various surface tension parameter λ , we show the fingering pattern where smaller surface tension contributes a larger number of fingering structures. These numerical simulations are qualitatively consistent with the numerical simulations in [51] and the experimental results in [54,55].

We continue to perform a simulation in 3D and set the computed domain as $(x, y, z) \in \Omega = [0, 2\pi] \times [0, 2\pi] \times [0, 0.6]$. The initial conditions read as (shown in the first subfigure of Fig. 4.13):

$$\phi^{0} = \tanh(\frac{r - \sqrt{(x - \pi)^{2} - (y - \pi)^{2} + (z + 1.05)^{2}}}{\epsilon}),$$

$$\mathbf{u}^{0} = (0, 0, 0), p^{0} = 0,$$
(4.9)

where r=1.5+0.01rand(\mathbf{x}). We assume periodic boundary conditions for the x and y-directions which are then discretized by using 512 Fourier-modes for each direction. The boundary conditions along the z-direction read as $(p_z, \phi_z, \mu_z)|_{(z=0,0.6)}=0$. The spatial discretization for z-direction is based on the Legendre–Galerkin method and the Legendre polynomials with degrees up

to 256 are used. The order parameters are still from (4.8). In Fig. 4.13, we plot the isosurfaces of $\{\phi=0\}$ at different times which clearly display that plenty of 3D fingers are formed over time. In Fig. 4.14, we vary the surface tension parameter λ , and find that the magnitude of λ directly affects the number of fingers, which is consistent with the 2D simulations, with a small surface tension causes more fingers. Similar dynamics were also observed experimentally/numerically in [51,54,55].

5. Concluding remarks

For the coupled nonlinear Cahn–Hilliard–Darcy phase-field model of Hele–Shaw flow, we have developed a novel and effective scheme in this paper. The novelty of the developed scheme is in the design of a special ODE to deal with the coupled nonlinear terms by utilizing their "zero-energy-contribution" characteristic. The combination of the new decoupling method, the projection method for the Darcy equations, and the AV method to linearize the nonlinear double-well potential leads to a fully-decoupled, linear, second-order accurate, unconditionally energy stable scheme. We give a detailed practical implementation and also prove the unconditional energy stability rigorously. By simulating a large number of 2D and 3D numerical examples and comparing them with several other known methods, we numerically prove the effectiveness of the developed scheme.

Declaration of competing interest

The authors declare that they have no known competing financial interests or personal relationships that could have appeared to influence the work reported in this paper.

Acknowledgment

X. Yang was partially supported by National Science Foundation, USA with grant numbers DMS-1720212, DMS-1818783, and DMS-2012490.

References

- [1] H.-G. Lee, J. Lowengrub, J. Goodman, Phys. Fluids 14 (2002) 492-513.
- [2] H. Garcke, K. Lam, On a Cahn-Hilliard-Darcy System for Tumour Growth with Solution Dependent Source Terms, Springer International Publishing, 2018, pp. 243–264.
- [3] G. Harald, L.F. Kei, S. Emanuel, S. Vanessa, Math. Models Methods Appl. Sci. 26 (2016) 1095–1148.
- [4] X. Feng, A. Prohl, Numer. Math. 94 (2003) 33-65.
- [5] J. Shen, X. Yang, Discrete Contin. Dyn. Syst. 28 (2010) 1669–1691.
- [6] J. Shen, C. Wang, S. Wang, X. Wang, SIAM J. Numer. Anal. 50 (2012) 105–125.
- [7] D.J. Eyre, Computational and Mathematical Models of Microstructural Evolution (San Francisco, CA, 1998), in: Mater. Res. Soc. Sympos. Proc., vol. 529, MRS, 1998, pp. 39–46.
- [8] S.M. Wise, C. Wang, J.S. Lowengrub, SIAM J. Numer. Anal. 47 (3) (2009) 2269–2288.
- [9] Z. Hu, S.M. Wise, C. Wang, J.S. Lowengrub, J. Comput. Phys. 228 (2009) 5323–5339.
- [10] D. Han, X. Wang, J. Comput. Phys. 290 (2015) 139-156.
- 11] D. Han, X. Wang, Numer. Methods Partial Differential Equations 32 (3) (2016) 936–954.
- [12] H. Yu, X. Yang, J. Comput. Phys. 334 (2017) 665-686.
- [13] J. Shen, X. Yang, SIAM J. Numer. Anal. 53 (1) (2015) 279–296.
- [14] X. Yang, H. Yu, SIAM J. Sci. Comput. 40 (2018) B889-B914.
- [15] X. Yang, J. Zhao, Q. Wang, J. Shen, Math. Models Methods Appl. Sci. 27 (2017) 1993–2030.
- [16] X. Yang, J. Comput. Phys. 327 (2016) 294–316.
- [17] C. Chen, X. Yang, J. Comput. Phys. 388 (2019) 41–62.
- [18] C. Chen, X. Yang, Comput. Methods Appl. Mech. Engrg. 351 (2019) 35–59.
- [19] Z. Yang, S. Dong, J. Comput. Phys. 393 (2018) 229–257.
- [20] J. Shen, X. Yang, Contemp. Math. 754 (2020) 217-245.
- [21] Q. Du, R.A. Nicolaides, SIAM J. Numer. Anal. 28 (1991) 1310–1322.

- [22] H. Gomez, der Zee Van, G. Kristoffer, Encyclopedia of Computational Mechanics, second ed., John Wiley & Sons, Ltd, 2017.
- [23] H. Gomez, V.M. Calo, Y. Bazilevs, T.J.R. Hughes, Comput. Methods Appl. Mech. Engrg. 197 (2008) 4333–4352.
- [24] I. Romero, Internat. J. Numer. Methods Engrg. 79 (2009) 706–732.
- [25] W. Chen, Y. Liu, C. Wang, S.M. Wise, Math. Comp. 85 (2016) 2231–2257.
- [26] X. Feng, S. Wise, SIAM J. Numer. Anal. 50 (2012) 1320-1343.
- [27] R. Nochetto, J.-H. Pyo, SIAM J. Numer. Anal. 43 (2005) 1043–1068.
- [28] D. Han, X. Wang, J. Sci. Comput. 14 (2018) 1210-1233.
- [29] R. Rannacher, The Navier-Stokes Equations II. Theory and Numerical Methods, in: Lecture Notes in Mathematics, vol. 1530, 1991, pp. 167–183.
- [30] J.L. Guermond, J. Shen, Math. Comp. 73 (2004) 1719-1737.
- [31] J.L. Guermond, A. Salgado, J. Comput. Phys. 228 (8) (2009) 2834–2846.
- [32] J.L. Guermond, L. Quartapelle, J. Comput. Phys. 165 (1) (2000) 167-188.
- [33] C. Liu, J. Shen, X. Yang, J. Sci. Comput. 62 (2015) 601–622.
- [34] J. Shen, X. Yang, SIAM J. Sci. Comput. 32 (2010) 1159-1179.
- [35] D. Han, A. Brylev, X. Yang, Z. Tan, J. Sci. Comput. 70 (2017) 965-989.
- [36] P. Lin, C. Liu, H. Zhang, J. Comput. Phys. 227 (2007) 1411–1427.
- [37] Y. Gong, J. Zhao, Q. Wang, SIAM J. Sci. Comput. 40 (2018) B528-B553.
- [38] X. Yang, J. Comput. Phys. 432 (2021) 110015.
- [39] X. Yang, Comput. Methods Appl. Mech. Engrg. 376 (2021) 13589.

- [40] X. Yang, Comput. Methods Appl. Mech. Engrg. 375 (2021) 113600.
- [41] X. Yang, Comput. Methods Appl. Mech. Engrg. 373 (2021) 113502.
- [42] X. Yang, Internat. J. Numer. Methods Engrg. 122 (2021) 1283-1306.
- [43] H. Abels, H. Garcke, G. Grün, Math. Models Methods Appl. Sci. 22 (3) (2012) 1150013. 40.
- [44] R.H. Nochetto, A.J. Salgado, I. Tomas., Comput. Methods Appl. Mech. Engrg. 309 (2016) 497-531.
- [45] B.I. Lev, V.G. Nazarenko, A.B. Nych, P.M. Tomchuk, JETP Lett. 71 (2000) 262–265.
- [46] R.H. Nochetto, A.J. Salgado, S.W. Walker, Math. Models Methods Appl. Sci. 24 (2014) 67-111.
- [47] X. Yang, Comput. Methods Appl. Mech. Engrg. 347 (2019) 316-339.
- [48] J. Bear, Dynamics of Fluids in Porous Media, Courier Dover Publications, New York, 1988.
- [49] D.A. Nield, A. Bejan, Convection in Porous Media, second ed., Springer-Verlag, New York, 1999.
- [50] J. Shen, Math. Comp. 65 (215) (1996) 1039–1065.
- [51] C.-Y. Chen, Y.-S. Huang, J.A. Miranda, Phys. Rev. E. 84 (2011) 046302.
- [52] J. Casademunt, Chaos 14 (2004) 809.
- [53] L. Carrillo, F.X. Magdaleno, J. Casademunt, J. Ortin, Phys. Rev. E 54 (1996) 6260.
- [54] E. Alvarez-Lacalle, J. Ortin, J. Casademunt, Phys. Fluids 16 (2004) 908–924.
- [55] E. Álvarez-Lacalle, J. Ortín, J. Casademunt, Phys. Rev. E 74 (2006) 025302.